

$n:m$ Phase-Locking of Heterogeneous and Strongly Coupled Oscillators

Youngmin Park^{*1}

¹*Department of Mathematics, University of Florida, Gainesville, FL 32611*

Abstract

We introduce a scalar reduction method beyond weak perturbations for forced or coupled systems to determine the existence and stability of $n:m$ phase-locked states affected by heterogeneity. We consider various biologically relevant oscillators including the complex Ginzburg-Landau oscillator, a thalamic neuron oscillator, and a model of circadian rhythms. The scalar reduction successfully captures the emergence and disappearance of phase-locked states as a function of coupling strength and heterogeneity. We find that even small amounts of heterogeneity (often orders of magnitude smaller than the coupling strength) can significantly alter phase-locked states. The proposed method is a straightforward means to both reduce and analyze potentially high dimensional systems of oscillators that exist closer to biologically-realistic settings.

1 Introduction

Coupled oscillators are ubiquitous in natural and physical systems such as the collective rhythms of pacemaker neurons in the nervous system [3, 39, 15, 21, 40], the walking pattern of crowds [35, 27], and chemical preparations [16, 6]. In particular, $n:m$ phase-locking, where one oscillator traverses n periods in the same time that the other coupled oscillator traverses m periods, is a natural feature of physical systems such as Microelectromechanical system oscillators [2], pulse-coupled cardiac pacemakers [25], and Belousov–Zhabotinsky chemical oscillators with asymmetric coupling [13].

Homogeneity and *symmetry* are common assumptions in the study of coupled oscillators that turn relatively complex models and behaviors into forms amenable to mathematical analyses. The Kuramoto oscillator is a classic example upon which significant progress has been made, such as the celebrated Ott-Antonsen ansatz [27], and recent fashionable works on n -body interactions [1]. Homogeneity and symmetry also allow detailed and general analytical studies of the existence and stability of $n:m$ phase-locked states for even strong coupling strengths and high dimensional oscillators, e.g., H/K theory [11] and firing time maps [4]. It is also common to start with particular models that are known to be analytically tractable, like the Van der pol oscillator [2], a circle map-like system [9], and the Rossler oscillator [5], to name a few.

However, in practice, *heterogeneity* is an inescapable feature that alters the behavior of coupled oscillators in the physical world. Experimental preparations of chemical

^{*}Corresponding author park.y@ufl.edu

oscillators with 3% variations in intrinsic frequencies disrupt the existence and stability of phase-locked states predicted using H/K theory [14]. Introducing heterogeneity in ecosystems models has been shown to stabilize phase dynamics from drift to locking [10, 24]. Biological neural networks, such as brains, do not consist of homogeneous neurons and exhibit high degrees of heterogeneity [34, 36]. Heterogeneity may even be a *necessary feature* of robust brain function [17]. While symmetry and homogeneity are exceptionally useful assumptions that have greatly advanced the field of coupled oscillators, the ubiquity of heterogeneity in nature warrants exploration in this direction. However, methods that include heterogeneity are relatively lacking.

We introduce methods to reduce a pair of $n:m$ coupled heterogeneous oscillators to relatively tractable equations in a manner similar to classic weak coupling theory (see, for example, [8, 30]). The proposed method uses a combination of phase and isostable coordinates employed in recent works [38, 37, 28, 31, 26]. The proposed method does not require oscillators to be strongly attracting (such as in [4]).

This paper has several objectives that we state here for concreteness:

- Explore the effects of heterogeneity on phase-locked states, and show that even very small degrees of heterogeneity may significantly alter the existence of phase-locking.
- Compare and contrast the phase-isostable reduction (which we call the “3D reduction” and is directly related to that studied by Nicks et al [26]) to the proposed scalar reduction (which we call the “1D reduction”) using various values of the coupling strength ε and heterogeneity δ , thus highlighting the utility of either approach.
- Show potential limits of both the phase-isostable reduction and the proposed scalar reduction in reproducing the existence and stability of phase-locked states for non-weak coupling strengths ε .

This paper is organized as follows. In Section 2, we introduce the assumptions on the types of vector fields amenable to the reduction, and derive the two types of model reductions we consider: the scalar reduction, where the isostable coordinates have been solved and are thus implicit in the reduction, and the 3D reduction, where the isostable coordinates are retained explicitly. The results, Section 3, are split into two parts, one for forcing results (Section 3.1), and one for coupling results (Section 3.2). We conclude with a discussion in Section 4.

2 Derivation

We seek phase-locked solutions of the coupled system

$$\begin{aligned} \frac{1}{\omega_X} \frac{dX}{dt} &= F_X(X) + \delta J_X(X) + \varepsilon G_X(X, Y), \\ \frac{1}{\omega_Y} \frac{dY}{dt} &= F_Y(Y) + \delta J_Y(Y) + \varepsilon G_Y(X, Y), \end{aligned} \tag{1}$$

where $F_i : \mathbb{R}^{n_i} \rightarrow \mathbb{R}^{n_i}$ is a smooth vector field, $J_i : \mathbb{R}^{n_i} \rightarrow \mathbb{R}^{n_i}$ is some additive heterogeneous term, $G_i : \mathbb{R}^{n_i} \times \mathbb{R}^{n_j} \rightarrow \mathbb{R}^{n_i}$ is a smooth coupling function, and $n_i \in \mathbb{N}$ for each oscillator $i = X, Y$. The scalar ε (not necessarily small) modulates the overall coupling strength of the network, and the scalar $\delta = O(\varepsilon)$ controls the magnitude of heterogeneity. In addition to smoothness, we assume,

- Each system in isolation admits a 2π -periodic limit cycle solution, $\Gamma_i(t_0 + 2\pi) = \Gamma_i(t_0)$ (where $t_0 \in \mathbb{R}$ is some arbitrary time shift), for $i = X, Y$.

- For $\varepsilon = 0$, the system (1) admits a pair of T_X - and T_Y -periodic solutions,

$$X_0(t) = \Gamma_X(\omega_X t), \quad Y_0(t) = \Gamma_Y(\omega_Y t),$$

where

$$nT_X = mT_Y, \quad \omega_X/\omega_Y = n/m, \quad T_X = 2\pi/\omega_X, \quad T_Y = 2\pi/\omega_Y.$$

That is, for every n oscillations traversed by oscillator X_0 , m oscillations are traversed by oscillator Y_0 .

- Limit cycles persist for $\varepsilon \neq 0$ and $\delta \neq 0$ in the coupled system (1).
- All Floquet eigenmodes decay rapidly except in one direction. We denote this nontrivial Floquet exponent by κ_X (κ_Y) for oscillator X (Y). Our calculations may be extended to the case of multiple nontrivial Floquet exponents so long as the nontrivial exponents are unique.

Remark 1. *While the assumption that both limit cycles have periods of exactly the ratio $n:m$ at $\varepsilon = \delta = 0$ may seem restrictive, this requirement is equivalent to asserting that it is possible to adjust the period of each system to have exactly such a ratio by adjusting parameters in each model (in neural models, a convenient parameter is the input current). Thus, the ratio $n:m$ does not necessarily imply a loss of generality.*

Remark 2. *We use one parameter for the strength of heterogeneity to simplify calculations, but the proposed method may be extended to any number of heterogeneous parameters $M_i \in \mathbb{N}$ for each oscillator i , e.g., δ_{ij} for $j = 1, \dots, M_i$, with possible nonlinear dependencies on δ_{ij} . Nonlinearities may be handled by truncating Taylor expansions in δ_{ij} . An example of such a formulation for $N \geq 2$ oscillators is discussed in [31].*

2.1 Phase-Isostable Reduction

To reduce the system into a set of lower-dimensional equations, we transform (1) into phase coordinates using the chain rule [37]:

$$\begin{aligned} \frac{d\theta_X}{dt} &= \omega_X \nabla \Theta_X \cdot [F_X(X) + \delta J_X(X) + \varepsilon G_X(X, Y)] \\ &= \omega_X [\nabla \Theta_X \cdot F_X(X) + \delta \nabla \Theta_X \cdot J_X(X) + \varepsilon \nabla \Theta_X \cdot G_X(X, Y)] \\ &= \omega_X [1 + \delta \mathcal{Z}_X(X) \cdot J_X(X) + \varepsilon \mathcal{Z}_X(X) \cdot G_X(X, Y)], \end{aligned} \quad (2)$$

where \mathcal{Z}_i is the general phase response function valid for stronger perturbations of the limit cycle beyond the linear regime [37]. Note that the solution X (Y) may be expressed purely in terms of phases θ_X (θ_Y) and isostables ψ_X (ψ_Y), but we keep (2) in terms of X and Y to keep the notation compact for now.

The remaining phase-isostable equations for (1) may be obtained using a similar chain rule argument (see, e.g., [37, 28, 31]):

$$\begin{aligned} \frac{1}{\omega_X} \frac{d\theta_X}{dt} &= 1 + \mathcal{Z}_X(X) \cdot [\delta J_X(X) + \varepsilon G_X(X, Y)], \\ \frac{1}{\omega_X} \frac{d\psi_X}{dt} &= \kappa_X \psi_X + \mathcal{I}_X(X) \cdot [\delta J_X(X) + \varepsilon G_X(X, Y)], \\ \frac{1}{\omega_Y} \frac{d\theta_Y}{dt} &= 1 + \mathcal{Z}_Y(Y) \cdot [\delta J_Y(Y) + \varepsilon G_Y(X, Y)], \\ \frac{1}{\omega_Y} \frac{d\psi_Y}{dt} &= \kappa_Y \psi_Y + \mathcal{I}_Y(Y) \cdot [\delta J_Y(Y) + \varepsilon G_Y(X, Y)]. \end{aligned} \quad (3)$$

To simplify calculations (and in the same spirit as [7]), we let $s = \omega_Y t$, transforming (3) to,

$$\begin{aligned}\frac{1}{\omega}\theta'_X &= 1 + \varepsilon \mathcal{Z}_X(X) \cdot \hat{G}_X(X, Y), \\ \frac{1}{\omega}\psi'_X &= \kappa_X \psi_X + \varepsilon \mathcal{I}_X(X) \cdot \hat{G}_X(X, Y), \\ \theta'_Y &= 1 + \varepsilon \mathcal{Z}_Y(Y) \cdot \hat{G}_Y(X, Y), \\ \psi'_Y &= \kappa_Y \psi_Y + \varepsilon \mathcal{I}_Y(Y) \cdot \hat{G}_Y(X, Y),\end{aligned}\tag{4}$$

where $' = d/ds$, $\omega := \omega_X/\omega_Y$, $b = \delta/\varepsilon$, $\hat{G}_X(X, Y) = bJ_X(X) + G_X(X, Y)$ and $\hat{G}_Y(X, Y) = bJ_Y(Y) + G_Y(X, Y)$. Because δ is at most order $O(\varepsilon)$, b is at most order $O(1)$. Note that we treat \hat{G}_i , the sum of G_i and heterogeneity, as a coupling function to simplify the notation when performing the calculations to follow. However, we will be careful to treat \hat{G} and G as distinct functions, because δ can significantly alter phase-locking dynamics. We briefly discuss the consequences of having such a heterogeneity term in analytical calculations at the end of Section 2.2.1.

By proceeding similarly to [28, 31, 26] we derive averaged phase and isostable coordinates by expanding all terms in ψ and plugging them into (4). The expansions are given by,

$$\mathcal{Z}_i(\theta, \psi) \approx Z_i^{(0)}(\theta) + \psi Z_i^{(1)}(\theta) + \psi^2 Z_i^{(2)}(\theta) + \dots, \tag{5}$$

$$\mathcal{I}_i(\theta, \psi) \approx I_i^{(0)}(\theta) + \psi I_i^{(1)}(\theta) + \psi^2 I_i^{(2)}(\theta) + \dots, \tag{6}$$

$$X(t) \approx X_0(\theta_X) + \psi_X g_X^{(1)}(\theta_X) + \psi_X^2 g_X^{(2)}(\theta_X) + \dots, \tag{7}$$

$$Y(t) \approx Y_0(\theta_Y) + \psi_Y g_Y^{(1)}(\theta_Y) + \psi_Y^2 g_Y^{(2)}(\theta_Y) + \dots, \tag{8}$$

where $i = X, Y$, and the functions $Z_i^{(k)}$, $I_i^{(k)}$, and $g_i^{(k)}$ are the higher-order correction terms to the infinitesimal phase response curve ($Z_i^{(0)}$), infinitesimal isostable response curve ($I_i^{(0)}$), and Floquet eigenfunction ($g_i^{(1)}$), respectively. These correction terms may be computed with high accuracy and to high orders using straightforward numerical methods [37, 32]. Then an expansion of g in ψ may be obtained as shown in Appendix A.

We now subtract the moving frame using $\hat{\theta}_X = \theta_X - \omega s$ and $\hat{\theta}_Y = \theta_Y - s$ and plug in the above expansions (5)–(8) into (4), arriving at the phase-isostable equations with a subtracted moving frame:

$$\begin{aligned}\frac{1}{\omega}\hat{\theta}'_X &= \varepsilon \mathcal{Z}_X(\hat{\theta}_X + \omega s, \psi_X) \cdot \hat{G}_X(\hat{\theta}_X + \omega s, \hat{\theta}_Y + s, \psi_X, \psi_Y), \\ \frac{1}{\omega}\psi'_X &= \kappa_X \psi_X + \varepsilon \mathcal{I}_X(\hat{\theta}_X + \omega s, \psi_X) \cdot \hat{G}_X(\hat{\theta}_X + \omega s, \hat{\theta}_Y + s, \psi_X, \psi_Y), \\ \hat{\theta}'_Y &= \varepsilon \mathcal{Z}_Y(\hat{\theta}_Y + s, \psi_Y) \cdot \hat{G}_Y(\hat{\theta}_X + \omega s, \hat{\theta}_Y + s, \psi_X, \psi_Y), \\ \psi'_Y &= \kappa_Y \psi_Y + \varepsilon \mathcal{I}_Y(\hat{\theta}_Y + s, \psi_Y) \cdot \hat{G}_Y(\hat{\theta}_X + \omega s, \hat{\theta}_Y + s, \psi_X, \psi_Y),\end{aligned}\tag{9}$$

Assumption 1. *We assume that the moving-frame subtracted phase variables, $\hat{\theta}_i$, evolve on a relatively slow timescale compared to the time variable s .*

This assumption allows us to apply first-order averaging to (9), yielding the averaged

system,

$$\begin{aligned}
\frac{1}{\omega} \hat{\theta}'_X &= \varepsilon \sum_{\ell=0}^M \psi_X^\ell \mathcal{F}_X^{(\ell)}(\hat{\theta}_X, \hat{\theta}_Y, \psi_X, \psi_Y), \\
\frac{1}{\omega} \psi'_X &= \kappa_X \psi_X + \varepsilon \sum_{\ell=0}^M \psi_X^\ell \mathcal{G}_X^{(\ell)}(\hat{\theta}_X, \hat{\theta}_Y, \psi_X, \psi_Y), \\
\hat{\theta}'_Y &= \varepsilon \sum_{\ell=0}^M \psi_Y^\ell \mathcal{F}_Y^{(\ell)}(\hat{\theta}_X, \hat{\theta}_Y, \psi_X, \psi_Y), \\
\psi'_Y &= \kappa_Y \psi_Y + \varepsilon \sum_{\ell=0}^M \psi_Y^\ell \mathcal{G}_Y^{(\ell)}(\hat{\theta}_X, \hat{\theta}_Y, \psi_X, \psi_Y),
\end{aligned} \tag{10}$$

where $M \in \mathbb{N}$ is some cutoff for the expansion in ψ_i and

$$\begin{aligned}
\mathcal{F}_i^{(\ell)} &= \sum_{j+k=\ell} \frac{\psi_i^j}{2\pi m} \int_0^{2\pi m} Z_i^{(j)}(\hat{\theta}_i + \omega s', \psi_i) \cdot \bar{K}_i^{(k)}(\hat{\theta}_X + \omega s', \hat{\theta}_Y + s', \psi_X, \psi_Y) ds', \\
\mathcal{G}_i^{(\ell)} &= \sum_{j+k=\ell} \frac{\psi_i^j}{2\pi m} \int_0^{2\pi m} I_i^{(j)}(\hat{\theta}_i + \omega s', \psi_i) \cdot \bar{K}_i^{(k)}(\hat{\theta}_X + \omega s', \hat{\theta}_Y + s', \psi_X, \psi_Y) ds'.
\end{aligned}$$

Thus we obtain our first reduction, which consist of both phase and isostable coordinates. We refer to (10) as the **phase-isostable** reduction (note that we abuse terminology for the sake of brevity – the phase-isostable equation as typically used in the literature is given by (3)). For a more elegant form of (10) to first-order in ψ_i , we refer the reader to Equation (18) in [26].

2.2 Scalar Reduction: Elimination of Isostable Coordinates

In some cases, we may wish to solve the isostable coordinates to reduce the dimension of the reduced system from 4 to 2 (see the Discussion in Section 4 for caveats of this approach). To do this, we must further expand all ψ_i variables in ε :

$$\psi_i(t) \approx \varepsilon p_i^{(1)}(t) + \varepsilon^2 p_i^{(2)}(t) + \varepsilon^3 p_i^{(3)}(t) + \dots \tag{11}$$

The expansion of ψ_i in the coupling strength ε is an ansatz. With this expansion in hand, we can now expand all functions in ε by plugging in (11) into each expansion in ψ . This process allows us to write an ε -expansion for the heterogeneity functions J_i :

$$J_i \approx J_i^{(0)} + \varepsilon J_i^{(1)} + \varepsilon^2 J_i^{(2)} + \dots,$$

which is a consequence of substituting the expansion of the solutions (7) and (8) and then substituting (11) into J_i in (1) and collecting in powers of ε . The ε -expansion of each coupling function G_i proceeds similarly, with additional details provided in Appendix A. We write the ε -expansion of G_X as

$$\begin{aligned}
G_X(\theta_X, \psi_X, \theta_Y, \psi_Y) &= K_X^{(0)}(\theta_X, \theta_Y) + \varepsilon K_X^{(1)}\left(\theta_X, \theta_Y, p_X^{(1)}, p_Y^{(1)}\right) \\
&\quad + \varepsilon^2 K_X^{(2)}\left(\theta_X, \theta_Y, p_X^{(1)}, p_X^{(2)}, p_Y^{(1)}, p_Y^{(2)}\right) \\
&\quad + \varepsilon^3 K_X^{(3)}\left(\theta_X, \theta_Y, p_X^{(1)}, p_X^{(2)}, p_X^{(3)}, p_Y^{(1)}, p_Y^{(2)}, p_Y^{(3)}\right) \\
&\quad + \dots,
\end{aligned} \tag{12}$$

where each K_X is computed in a manner similar to J_i . The ε -expansion of G_Y is virtually identical in form to (12) with the exception of some indices (Appendix A).

While we now have all the necessary expansions in ε to rewrite the phase-amplitude equations (4) in powers of ε , there are still two variables for each oscillator, namely θ_i and ψ_i , for $i = X, Y$. Thus, some work remains to reduce each oscillator into a single phase difference variable.

We proceed with the method suggested by [38, 28, 31] and derive linear equations for each term $p_i^{(k)}$ in the expansion of ψ_i (11) in terms of $\hat{\theta}_{X,Y}$. Recall (9), the phase-isostables prior to averaging but after subtracting the moving frame(s), which we rewrite here for convenience:

$$\frac{1}{\omega} \hat{\theta}'_X = \varepsilon \mathcal{Z}_X(\hat{\theta}_X + \omega s, \psi_X) \cdot \hat{G}_X(\hat{\theta}_X + \omega s, \hat{\theta}_Y + s, \psi_X, \psi_Y), \quad (13)$$

$$\frac{1}{\omega} \psi'_X = \kappa_X \psi_X + \varepsilon \mathcal{I}_X(\hat{\theta}_X + \omega s, \psi_X) \cdot \hat{G}_X(\hat{\theta}_X + \omega s, \hat{\theta}_Y + s, \psi_X, \psi_Y), \quad (14)$$

for X and

$$\hat{\theta}'_Y = \varepsilon \mathcal{Z}_Y(\hat{\theta}_Y + s, \psi_Y) \cdot \hat{G}_Y(\hat{\theta}_X + \omega s, \hat{\theta}_Y + s, \psi_X, \psi_Y), \quad (15)$$

$$\psi'_Y = \kappa_Y \psi_Y + \varepsilon \mathcal{I}_Y(\hat{\theta}_Y + s, \psi_Y) \cdot \hat{G}_Y(\hat{\theta}_X + \omega s, \hat{\theta}_Y + s, \psi_X, \psi_Y), \quad (16)$$

for Y . We now proceed to eliminate the isostable coordinates ψ_i .

2.2.1 Integration of Isostable Coordinates

We substitute the expansion $\psi_i(s) = \varepsilon p_i^{(1)}(s) + \varepsilon^2 p_i^{(2)}(s) + \varepsilon^3 p_i^{(3)}(s) + \dots$ into (14) and (16) to obtain a hierarchy of ODEs for ψ_i in powers of ε . The left-hand side consists of straightforward time derivatives:

$$\begin{aligned} \frac{1}{\omega} \frac{d}{ds} \psi_X &= \frac{\varepsilon}{\omega_X} \frac{d}{ds} p_X^{(1)} + \frac{\varepsilon^2}{\omega} \frac{d}{ds} p_X^{(2)} + \frac{\varepsilon^3}{\omega} \frac{d}{ds} p_X^{(3)} + \dots, \\ \frac{d}{ds} \psi_Y &= \varepsilon \frac{d}{ds} p_Y^{(1)} + \varepsilon^2 \frac{d}{ds} p_Y^{(2)} + \varepsilon^3 \frac{d}{ds} p_Y^{(3)} + \dots, \end{aligned}$$

and the right-hand side includes numerous cross-multiplication terms. For ψ_X we have,

$$\begin{aligned} &\kappa_X \psi_X + \varepsilon \mathcal{I}_X(\hat{\theta}_X + \omega s, \psi_X) \cdot \hat{G}_X(\hat{\theta}_X + \omega s, \hat{\theta}_Y + s, \psi_X, \psi_Y) \\ &= \kappa_X \left(\varepsilon p_X^{(1)} + \varepsilon^2 p_X^{(2)} + \varepsilon^3 p_X^{(3)} + \dots \right) \\ &\quad + \varepsilon \left[I_X^{(0)}(\hat{\theta}_X + \omega s) + \psi_X I_X^{(1)}(\hat{\theta}_X + \omega s) + \psi_X^2 I_X^{(2)}(\hat{\theta}_X + \omega s) + \dots \right] \\ &\quad \cdot \left[\hat{K}_X^{(0)}(\hat{\theta}_X + \omega s, \hat{\theta}_Y + s) + \varepsilon \hat{K}_X^{(1)}(\hat{\theta}_X + \omega s, \hat{\theta}_Y + s, p_X^{(1)}, p_Y^{(1)}) \right. \\ &\quad \left. + \varepsilon^2 \hat{K}_X^{(2)}(\hat{\theta}_X + \omega s, \hat{\theta}_Y + s, p_X^{(1)}, p_X^{(2)}, p_Y^{(1)}, p_Y^{(2)}) \right. \\ &\quad \left. + \varepsilon^3 \hat{K}_X^{(3)}(\hat{\theta}_X + \omega s, \hat{\theta}_Y + s, p_X^{(1)}, p_X^{(2)}, p_X^{(3)}, p_Y^{(1)}, p_Y^{(2)}, p_Y^{(3)}) + \dots \right]. \end{aligned}$$

For ψ_Y ,

$$\begin{aligned}
& \kappa_Y \psi_Y + \varepsilon \mathcal{I}_Y(\hat{\theta}_Y + s, \psi_Y) \cdot \hat{G}_Y(\hat{\theta}_X + \omega s, \hat{\theta}_Y + s, \psi_X, \psi_Y) \\
&= \kappa_Y \left(\varepsilon p_Y^{(1)} + \varepsilon^2 p_Y^{(2)} + \varepsilon^3 p_Y^{(3)} + \dots \right) \\
&+ \varepsilon \left[I_Y^{(0)}(\hat{\theta}_Y + s) + \psi_Y I_Y^{(1)}(\hat{\theta}_Y + s) + \psi_Y^2 I_Y^{(2)}(\hat{\theta}_Y + s) + \dots \right] \\
&\quad \cdot \left[\hat{K}_Y^{(0)}(\hat{\theta}_X + \omega s, \hat{\theta}_Y + s) + \varepsilon \hat{K}_Y^{(1)}(\hat{\theta}_X + \omega s, \hat{\theta}_Y + s, p_X^{(1)}, p_Y^{(1)}) \right. \\
&\quad + \varepsilon^2 \hat{K}_Y^{(2)}(\hat{\theta}_X + \omega s, \hat{\theta}_Y + s, p_X^{(1)}, p_X^{(2)}, p_Y^{(1)}, p_Y^{(2)}) \\
&\quad \left. + \varepsilon^3 \hat{K}_Y^{(3)}(\hat{\theta}_X + \omega s, \hat{\theta}_Y + s, p_X^{(1)}, p_X^{(2)}, p_X^{(3)}, p_Y^{(1)}, p_Y^{(2)}, p_Y^{(3)}) + \dots \right].
\end{aligned}$$

Re-collecting in powers of ε yields a hierarchy of scalar ODEs, which we show up to order ε^3 in (17) below. For notational clarity, we suppress the explicit θ_{i-} , θ_{j-} and $p_i^{(k)}$ -dependence of the functions $I^{(k)}$, $\hat{K}^{(k)}$, and $p_i^{(k)}$, and the time dependence of $p_i^{(k)}$.

$$\begin{aligned}
\frac{1}{\omega} \frac{dp_X^{(1)}}{ds} &= \kappa_X p_X^{(1)} + I_X^{(0)} \cdot \hat{K}_X^{(0)}, \\
\frac{1}{\omega} \frac{dp_X^{(2)}}{ds} &= \kappa_X p_X^{(2)} + I_X^{(0)} \cdot \hat{K}_X^{(1)} + p_X^{(1)} I_X^{(1)} \cdot \hat{K}_X^{(0)}, \\
\frac{1}{\omega} \frac{dp_X^{(3)}}{ds} &= \kappa_X p_X^{(3)} + I_X^{(0)} \cdot \hat{K}_X^{(2)} + p_X^{(1)} I_X^{(1)} \cdot \hat{K}_X^{(1)} + p_X^{(2)} I_X^{(1)} \cdot \hat{K}_X^{(0)} + \left(p_X^{(1)} \right)^2 I_X^{(2)} \cdot \hat{K}_X^{(0)}, \\
&\vdots
\end{aligned} \tag{17}$$

Similarly,

$$\begin{aligned}
\frac{dp_Y^{(1)}}{ds} &= \kappa_Y p_Y^{(1)} + I_Y^{(0)} \cdot \hat{K}_Y^{(0)}, \\
\frac{dp_Y^{(2)}}{ds} &= \kappa_Y p_Y^{(2)} + I_Y^{(0)} \cdot \hat{K}_Y^{(1)} + p_Y^{(1)} I_Y^{(1)} \cdot \hat{K}_Y^{(0)}, \\
\frac{dp_Y^{(3)}}{ds} &= \kappa_Y p_Y^{(3)} + I_Y^{(0)} \cdot \hat{K}_Y^{(2)} + p_Y^{(1)} I_Y^{(1)} \cdot \hat{K}_Y^{(1)} + p_Y^{(2)} I_Y^{(1)} \cdot \hat{K}_Y^{(0)} + \left(p_Y^{(1)} \right)^2 I_Y^{(2)} \cdot \hat{K}_Y^{(0)}, \\
&\vdots
\end{aligned} \tag{18}$$

All ODEs are first-order inhomogeneous differential equations with forcing terms that depend on lower-order solutions. As such, we can solve each ODE explicitly (in practice, we pre-compute the functions $p_i^{(\ell)}$ so that they are not computed on the fly like in the phase-isostable reduction (10)). For an arbitrary order $O(\varepsilon^k)$, the equation to be solved is given by,

$$\begin{aligned}
\frac{1}{\omega} \frac{dp_X^{(k)}}{ds} &= \kappa_X p_X^{(k)} + f_X^{(k)}(\theta_X, \theta_Y, \{p_X^{(\ell)}(s)\}_{\ell=1}^{(k-1)}, \{p_Y^{(\ell)}(s)\}_{\ell=1}^{(k-1)}), \\
\frac{dp_Y^{(k)}}{ds} &= \kappa_Y p_Y^{(k)} + f_Y^{(k)}(\theta_X, \theta_Y, \{p_X^{(\ell)}(s)\}_{\ell=1}^{(k-1)}, \{p_Y^{(\ell)}(s)\}_{\ell=1}^{(k-1)}),
\end{aligned}$$

where the forcing functions are the inhomogeneous terms in (17) and (18). The inputs $\{p_X^{(\ell)}(s)\}_{\ell=1}^{(k-1)}$ and $\{p_Y^{(\ell)}(s)\}_{\ell=1}^{(k-1)}$ are short-hand denoting that each forcing function $f_i^{(k)}$ depends on all $p_X^{(\ell)}$ and $p_Y^{(\ell)}$ solutions up to order $\ell = k - 1$.

The solution to each equation is straightforward to compute with a combination of symbolic and numerical methods, but for clarity we explicitly show how the solution is computed using the first term in (17) (identical logic follows for (18)). The first term is rewritten here for convenience:

$$\frac{1}{\omega} \frac{d}{ds} p_X^{(1)}(s) = \kappa_X p_X^{(1)}(s) + I_X^{(0)}(\hat{\theta}_X + \omega s) \cdot \hat{K}_X^{(0)}(\hat{\theta}_X + \omega s, \hat{\theta}_Y + s).$$

The solution (including transients) may be found using standard methods:

$$p_X^{(1)}(s) = \omega \int_0^s e^{\omega \kappa_X (s-r)} I_X^{(0)}(\hat{\theta}_X + \omega r) \cdot \hat{K}_X^{(0)}(\hat{\theta}_X + \omega r, \hat{\theta}_Y + r) dr + p_X^{(1)}(0) e^{\omega \kappa_X s}.$$

Assumption 2. For each fixed $\hat{\theta}_X, \hat{\theta}_Y$, each $p_i^{(\ell)}$ term has transients that may be safely ignored and reaches a steady-state value (as opposed to long-term behavior exhibiting oscillations or chaos).

This assumption allows us to rewrite domain of integration from $[0, s]$ to $(-\infty, s]$ and drop the initial condition:

$$p_X^{(1)}(s) = \omega \int_{-\infty}^s e^{\omega \kappa_X (s-r)} I_X^{(0)}(\hat{\theta}_X + \omega r) \cdot \hat{K}_X^{(0)}(\hat{\theta}_X + \omega r, \hat{\theta}_Y + r) dr.$$

With the change of variables $r' = s - r$, the above equation becomes

$$p_X^{(1)}(s) = \omega \int_0^{\infty} e^{\omega \kappa_X r} I_X^{(0)}(\hat{\theta}_X + \omega(s-r)) \cdot \hat{K}_X^{(0)}(\hat{\theta}_X + \omega(s-r), \hat{\theta}_Y + s-r) dr.$$

By definition, this term may be viewed purely as a function of θ_X, θ_Y :

$$p_X^{(1)}(\theta_X, \theta_Y) = \omega \int_0^{\infty} e^{\omega \kappa_X r} I_X^{(0)}(\theta_X - \omega r) \cdot \hat{K}_X^{(0)}(\theta_X - r\omega, \theta_Y - r) dr,$$

and by an identical argument,

$$p_Y^{(1)}(\theta_X, \theta_Y) = \int_0^{\infty} e^{\kappa_Y r} I_Y^{(0)}(\theta_Y - r) \cdot \hat{K}_Y^{(0)}(\theta_X - r\omega, \theta_Y - r) dr.$$

Because $p_X^{(1)}$ and $p_Y^{(1)}$ only depend on phase variables, these functions may be pre-computed numerically. The numerical computation can be made especially efficient by rewriting the above as a 1D convolution. The transformation is performed by fixing some $c \in [0, 2\pi)$ such that $\theta_X = c + \theta_Y \omega$. Then,

$$\begin{aligned} p_X^{(1)}(c + \theta_Y \omega, \theta_Y) &= \omega \int_0^{\infty} e^{\omega \kappa_X r} I_X^{(0)}(c + \omega(\theta_Y - r)) \cdot \hat{K}_X^{(0)}(c + \omega(\theta_Y - r), \theta_Y - r) dr \\ &= \omega \int_{-\infty}^{\infty} H(r) e^{\omega \kappa_X r} I_X^{(0)}(c + \omega(\theta_Y - r)) \cdot \hat{K}_X^{(0)}(c + \omega(\theta_Y - r), \theta_Y - r) dr \\ &= \omega [H(\theta_Y) e^{\omega \kappa_X \theta_Y}] * f_{X,c}(\theta_Y), \end{aligned}$$

where $f_{X,c}(\theta_Y) = I_X^{(0)}(c + \omega \theta_Y) \cdot \hat{K}_X^{(0)}(c + \omega \theta_Y, \theta_Y)$ and $*$ is the convolution operator. Similarly,

$$p_Y^{(1)}(c + \theta_Y \omega, \theta_Y) = [H(\theta_Y) e^{\kappa_Y \theta_Y}] * f_{Y,c}(\theta_Y),$$

where $f_{Y,c}(\theta_Y) = I_Y^{(0)}(c + \omega\theta_Y) \cdot \hat{K}_Y^{(0)}(c + \omega\theta_Y, \theta_Y)$.

When we solve $p_X^{(2)}$ ($p_Y^{(2)}$) for order $k = 2$, the forcing function includes the term $p_X^{(1)}(\theta_X, \theta_Y)$ ($p_Y^{(1)}(\theta_X, \theta_Y)$), which may be integrated in the same manner as above to solve for $p_X^{(2)}$ ($p_Y^{(2)}$). Indeed, we may precompute as many higher-order terms $p_X^{(\ell)}(\theta_X, \theta_Y)$, $p_Y^{(\ell)}(\theta_X, \theta_Y)$ as needed, thus obtaining explicit terms for the coefficients of the expansion $\psi_X = \varepsilon p_X^{(1)} + \varepsilon^2 p_X^{(2)} + \dots$ ($\psi_Y = \varepsilon p_Y^{(1)} + \varepsilon^2 p_Y^{(2)} + \dots$), effectively eliminating the ψ_X (ψ_Y) equations (while retaining their non-transient dynamics).

Remark 3. *The heterogeneity parameter b appears in each solution $p_X^{(\ell)}$ (or $p_Y^{(\ell)}$) up to the power b^ℓ .*

The intuition behind this remark is straightforward to confirm by taking $J_X = (1, 0, \dots, 0)^\top$, and $J_Y = 0$ so that the heterogeneity parameter b only appears in the first coordinate in oscillator X . Then, $\hat{K}_X^{(0)} = K_X^{(0)} + (b, 0, \dots, 0)^\top$ and $\hat{K}_X^{(\ell)} = K_X^{(\ell)}$ for $\ell \geq 1$. With this choice of heterogeneity, the solution of $p_X^{(1)}$ will have an additive term scaled by b . It then follows that the right-hand side of $p_X^{(2)}$, which contains the term $p_X^{(1)} I_X^{(1)} \cdot (K_X^{(0)} + (b, 0, \dots, 0)^\top)$, will contain a b^2 term. It is possible to argue inductively to higher powers. We rely on automated symbolic manipulation to handle these calculations for us, but we refer the reader to the derivation in [31] for additional details, including the case where $N \geq 2$ oscillators.

2.2.2 Phase Difference Equation

Assumption 1 (sufficient separation of timescales) places an existence on the upper bound in ε for which the proposed reduction method is valid. As our results will show, higher-order averaging and a significant timescale separation is not necessary for the reduced equations to capture nonlinear effects in the coupling strength ε . However, if needed, we will utilize higher-order averaging from, e.g., [18, 19] in future work.

We now obtain a phase difference equation for each order in ε . To provide a bird's-eye view, we perform the average,

$$\begin{aligned} \frac{1}{\omega} \hat{\theta}'_X &= \frac{1}{2\pi m} \int_0^{2\pi m} \mathcal{Z}_X(\hat{\theta}_X + \omega s, \hat{\theta}_Y + s) \cdot \hat{G}_X(\hat{\theta}_X + \omega s, \hat{\theta}_Y + s) ds, \\ \hat{\theta}'_Y &= \frac{1}{2\pi m} \int_0^{2\pi m} \mathcal{Z}_Y(\hat{\theta}_X + \omega s, \hat{\theta}_Y + s) \cdot \hat{G}_Y(\hat{\theta}_X + \omega s, \hat{\theta}_Y + s) ds, \end{aligned}$$

where we momentarily abuse notation and let $\hat{\theta}_i$ denote the averaged version of the variables θ_i and do not explicitly include the ψ_i terms because they are included implicitly. By applying the transformation $s \rightarrow \theta_Y + s$, we arrive at a more convenient form,

$$\begin{aligned} \frac{1}{\omega} \hat{\theta}'_X &= \frac{1}{2\pi m} \int_0^{2\pi m} \mathcal{Z}_X(\hat{\theta}_X - \omega\hat{\theta}_Y + \omega s, s) \cdot \hat{G}_X(\hat{\theta}_X - \omega\hat{\theta}_Y + \omega s, s) ds, \\ \hat{\theta}'_Y &= \frac{1}{2\pi m} \int_0^{2\pi m} \mathcal{Z}_Y(\hat{\theta}_X - \omega\hat{\theta}_Y + \omega s, s) \cdot \hat{G}_Y(\hat{\theta}_X - \omega\hat{\theta}_Y + \omega s, s) ds. \end{aligned}$$

These equations are useful because the integrals can now be expressed as functions of the phase difference $\phi = \hat{\theta}_X - \omega\hat{\theta}_Y$, which will further reduce the dimension of the system to a scalar equation. For the following calculations, we resume working with $bJ_X(X) + G_X(X, Y)$ ($bJ_Y(Y) + G_Y(X, Y)$) directly as opposed to $\hat{G}_X(X, Y)$ ($\hat{G}_Y(X, Y)$).

Substituting the expansion for ψ_X and collecting in powers of ε yields a virtually identical right-hand side as (17) with Z in place of I :

$$\begin{aligned}
\frac{1}{\omega} \hat{\theta}'_X &= Z_X^{(0)} \cdot K_X^{(0)} + \varepsilon \left(Z_X^{(0)} \cdot K_X^{(1)} + p_X^{(1)} Z_X^{(1)} \cdot K_X^{(0)} \right) \\
&+ \varepsilon^2 \left(Z_X^{(0)} \cdot K_X^{(2)} + p_X^{(1)} Z_X^{(1)} \cdot K_X^{(1)} + p_X^{(2)} Z_X^{(1)} \cdot K_X^{(0)} + \left(p_X^{(1)} \right)^2 Z_X^{(2)} \cdot K_X^{(0)} \right) \\
&+ \dots \\
&+ b Z_X^{(0)} \cdot J_X^{(0)} + \varepsilon b \left(Z_X^{(1)} J_X^{(0)} + Z_X^{(0)} J_X^{(1)} \right) \\
&+ \varepsilon^2 b \left(Z_X^{(2)} J_X^{(0)} + Z_X^{(1)} J_X^{(1)} + Z_X^{(0)} J_X^{(2)} \right) \\
&+ \dots,
\end{aligned} \tag{19}$$

Similarly,

$$\begin{aligned}
\hat{\theta}'_Y &= Z_Y^{(0)} \cdot K_Y^{(0)} + \varepsilon \left(Z_Y^{(0)} \cdot K_Y^{(1)} + p_Y^{(1)} Z_Y^{(1)} \cdot K_Y^{(0)} \right) \\
&+ \varepsilon^2 \left(Z_Y^{(0)} \cdot K_Y^{(2)} + p_Y^{(1)} Z_Y^{(1)} \cdot K_Y^{(1)} + p_Y^{(2)} Z_Y^{(1)} \cdot K_Y^{(0)} + \left(p_Y^{(1)} \right)^2 Z_Y^{(2)} \cdot K_Y^{(0)} \right) \\
&+ \dots \\
&+ b Z_Y^{(0)} \cdot J_Y^{(0)} + \varepsilon b \left(Z_Y^{(1)} J_Y^{(0)} + Z_Y^{(0)} J_Y^{(1)} \right) \\
&+ \varepsilon^2 b \left(Z_Y^{(2)} J_Y^{(0)} + Z_Y^{(1)} J_Y^{(1)} + Z_Y^{(0)} J_Y^{(2)} \right) \\
&+ \dots,
\end{aligned} \tag{20}$$

We average each $O(\varepsilon^\ell)$ term in (19) and (20), yielding a system of autonomous phase equations

$$\frac{1}{\omega} \theta'_X = b \sum_{\ell=1}^M \varepsilon^{\ell-1} \mathcal{J}_X^{(\ell)} + \sum_{\ell=1}^M \varepsilon^{\ell-1} \left[\mathcal{H}_X^{(\ell)} (\theta_X - \omega \theta_Y) \right], \tag{21}$$

$$\theta'_Y = b \sum_{\ell=1}^M \varepsilon^{\ell-1} \mathcal{J}_Y^{(\ell)} + \sum_{\ell=1}^M \varepsilon^{\ell-1} \left[\mathcal{H}_Y^{(\ell)} (\theta_X - \omega \theta_Y) \right], \tag{22}$$

where

$$\begin{aligned}
\mathcal{J}_i^{(1)} &= \frac{1}{2\pi} \int_0^{2\pi} Z_i^{(0)}(s) \cdot J_i^{(0)}(s) \, ds, \\
\mathcal{J}_i^{(2)} &= \frac{1}{2\pi} \int_0^{2\pi} Z_i^{(1)}(s) \cdot J_i^{(0)}(s) + Z_i^{(0)}(s) \cdot J_i^{(1)}(s) \, ds, \\
\mathcal{J}_i^{(3)} &= \frac{1}{2\pi} \int_0^{2\pi} Z_i^{(2)}(s) \cdot J_i^{(0)}(s) + Z_i^{(1)}(s) \cdot J_i^{(1)}(s) + Z_i^{(0)}(s) \cdot J_i^{(2)}(s) \, ds, \\
&\vdots
\end{aligned}$$

and

$$\begin{aligned}
\mathcal{H}_X^{(1)}(\xi) &= \frac{1}{2\pi m} \int_0^{2\pi m} Z_X^{(0)}(\xi + \omega s) \cdot K_X^{(0)}(\xi + \omega s, s) \, ds, \\
\mathcal{H}_X^{(2)}(\xi) &= \frac{1}{2\pi m} \int_0^{2\pi m} Z_X^{(0)}(\xi + \omega s) \cdot K_X^{(1)}(\xi + \omega s, \xi) \\
&\quad + p_X^{(1)}(\xi + \omega s, \xi) Z_X^{(1)}(\xi + \omega s) \cdot K_X^{(0)}(\xi + \omega s, \xi) \, ds, \\
\mathcal{H}_X^{(3)}(\xi) &= \frac{1}{2\pi m} \int_0^{2\pi m} Z_X^{(0)}(\xi + \omega s) \cdot K_X^{(2)}(\xi + \omega s, \xi) \\
&\quad + p_X^{(1)}(\xi + \omega s, \xi) Z_X^{(1)}(\xi + \omega s) \cdot K_X^{(1)}(\xi + \omega s, \xi) \\
&\quad + p_X^{(2)}(\xi + \omega s, \xi) Z_X^{(1)}(\xi + \omega s) \cdot K_X^{(0)}(\xi + \omega s, \xi) \\
&\quad + p_X^{(1)}(\xi + \omega s, \xi)^2 Z_X^{(2)}(\xi + \omega s) \cdot K_X^{(0)}(\xi + \omega s, \xi) \, ds, \\
&\quad \vdots
\end{aligned}$$

Similarly,

$$\begin{aligned}
\mathcal{H}_Y^{(1)}(\xi) &= \frac{1}{2\pi m} \int_0^{2\pi m} Z_Y^{(0)}(\xi + \omega s) \cdot K_Y^{(0)}(\xi + \omega s, \xi) \, ds, \\
\mathcal{H}_Y^{(2)}(\xi) &= \frac{1}{2\pi m} \int_0^{2\pi m} Z_Y^{(0)}(\xi + \omega s) \cdot K_Y^{(1)}(\xi + \omega s, \xi) \\
&\quad + p_Y^{(1)}(\xi + \omega s, \xi) Z_Y^{(1)}(\xi + \omega s) \cdot K_Y^{(0)}(\xi + \omega s, \xi) \, ds, \\
\mathcal{H}_Y^{(3)}(\xi) &= \frac{1}{2\pi m} \int_0^{2\pi m} Z_Y^{(0)}(\xi + \omega s) \cdot K_Y^{(2)}(\xi + \omega s, \xi) \\
&\quad + p_Y^{(1)}(\xi + \omega s, \xi) Z_Y^{(1)}(\xi + \omega s) \cdot K_Y^{(1)}(\xi + \omega s, \xi) \\
&\quad + p_Y^{(2)}(\xi + \omega s, \xi) Z_Y^{(1)}(\xi + \omega s) \cdot K_Y^{(0)}(\xi + \omega s, \xi) \\
&\quad + p_Y^{(1)}(\xi + \omega s, \xi)^2 Z_Y^{(2)}(\xi + \omega s) \cdot K_Y^{(0)}(\xi + \omega s, \xi) \, ds, \\
&\quad \vdots
\end{aligned}$$

Defining $\phi = \theta_X - \omega\theta_Y$, the corresponding ordinary differential equation is given by

$$\begin{aligned}
\phi' &= \theta'_X - \omega\theta'_Y \\
\phi' &= \omega b \sum_{\ell=1}^M \varepsilon^{\ell-1} \mathcal{J}_X^{(\ell)} + \omega \sum_{\ell=1}^M \varepsilon^{\ell-1} \mathcal{H}_X^{(\ell)}(\phi) \\
&\quad - \omega b \sum_{\ell=1}^M \varepsilon^{\ell-1} \mathcal{J}_Y^{(\ell)} - \omega \sum_{\ell=1}^M \varepsilon^{\ell-1} \mathcal{H}_Y^{(\ell)}(\phi).
\end{aligned}$$

Finally, defining $\mathcal{H}_{n,m}^{(\ell)}(\phi) = \mathcal{H}_X^{(\ell)}(\phi) - \mathcal{H}_Y^{(\ell)}(\phi)$, and $b^{(\ell)} = (\mathcal{J}_X^{(\ell)} - \mathcal{J}_Y^{(\ell)})b$, the phase difference dynamics is given by the scalar equation,

$$\frac{1}{\omega} \phi' = \sum_{\ell=1}^M \varepsilon^{\ell-1} [b^{(\ell)} + \mathcal{H}_{n,m}^{(\ell)}(\phi)]. \quad (23)$$

Remarks:

- In the coupling case, there is an implicit dependence on the heterogeneity term b inside the function $\mathcal{H}_{n,m}^{(\ell)}(\phi)$, because for nonzero b , each forcing function of $p_i^{(\ell)}$ will also contain b (up to the power b^ℓ).
- In the forcing case, changes to the forcing frequency simply results in a vertical shift of the $\mathcal{H}_{n,m}^{(\ell)}$ functions because the dependence on the heterogeneity parameter δ is completely described by (23) (see Section 3.1).
- If each $b^{(\ell)}$ is too large, e.g.,

$$|b^{(\ell)}| > \max_{\phi} |\mathcal{H}_{n,m}^{(\ell)}(\phi)|$$

for each ℓ , then there exist no equilibria in (23) and there can be no $n:m$ coupling. In such a case, the reduction exhibits phase drift (see the results in Section 3). However, it is possible to tune the heterogeneity parameter to find $b^{(\ell)}$ such that there exist equilibria. Thus, heterogeneity may induce phase drift or phase-locking depending on how it is chosen.

2.3 Summary of Reduced Models

Throughout this paper we consider the phase-isostable reduction (10), the scalar reduction (23), and the original dynamical system (1). Concurrent use of the phase-isostable and scalar reduction reveals the strengths and weaknesses of either approach. The reductions are rewritten here for convenience.

- **3D reduction** (Phase-isostable reduction, directly related to the reduction used by Nicks et al in [26])

$$\begin{aligned} \frac{1}{\omega} \phi' &= \varepsilon \sum_{\ell=0}^M \psi_X^\ell \mathcal{F}_X^{(\ell)}(\phi, \psi_X, \psi_Y) - \psi_Y^\ell \mathcal{F}_Y^{(\ell)}(\phi, \psi_X, \psi_Y), \\ \frac{1}{\omega} \psi_X' &= \kappa_X \psi_Y + \varepsilon \sum_{\ell=0}^M \psi_X^\ell \mathcal{G}_X^{(\ell)}(\phi, \psi_X, \psi_Y), \\ \psi_Y' &= \kappa_Y \psi_Y + \varepsilon \sum_{\ell=0}^M \psi_Y^\ell \mathcal{G}_Y^{(\ell)}(\phi, \psi_X, \psi_Y), \end{aligned} \quad (24)$$

where M is some cutoff for the expansion in ψ_i and

$$\begin{aligned} \mathcal{F}_X^{(\ell)} &= \sum_{j+k=\ell} \frac{\psi_X^\ell}{2\pi m} \int_0^{2\pi m} Z_X^{(j)}(\phi + \omega s', \psi_X) \cdot \bar{K}_X^{(k)}(\phi + \omega s', s', \psi_X, \psi_Y) ds', \\ \mathcal{G}_X^{(\ell)} &= \sum_{j+k=\ell} \frac{\psi_X^\ell}{2\pi m} \int_0^{2\pi m} I_X^{(j)}(\phi + \omega s', \psi_X) \cdot \bar{K}_X^{(k)}(\phi + \omega s', s', \psi_X, \psi_Y) ds', \end{aligned}$$

and similarly,

$$\begin{aligned} \mathcal{F}_Y^{(\ell)} &= \sum_{j+k=\ell} \frac{\psi_Y^\ell}{2\pi m} \int_0^{2\pi m} Z_Y^{(j)}(\phi + s', \psi_Y) \cdot \bar{K}_Y^{(k)}(\phi + \omega s', s', \psi_X, \psi_Y) ds', \\ \mathcal{G}_Y^{(\ell)} &= \sum_{j+k=\ell} \frac{\psi_Y^\ell}{2\pi m} \int_0^{2\pi m} I_Y^{(j)}(\phi + s', \psi_Y) \cdot \bar{K}_Y^{(k)}(\phi + \omega s', s', \psi_X, \psi_Y) ds', \end{aligned}$$

- **2D reduction** (phase-isostable reduction): What we call the 2D reduction is identical to the 3D reduction, but without the ψ_Y isostable coordinate. The 2D reduction appears in forcing.
- **1D reduction** (Scalar reduction, directly related to that used by Park and Wilson in [28, 31]):

$$\frac{1}{\omega_X} \frac{d\phi}{d\tau} = \sum_{\ell=1}^M \varepsilon^{\ell-1} [b^{(\ell)} + \mathcal{H}_{n,m}^{(\ell)}(\phi) + a^{(\ell)}], \quad (25)$$

where $b^{(\ell)} = (\mathcal{J}_X^{(\ell)} - \mathcal{J}_Y^{(\ell)})b$. Note that this 1D reduction, despite its name, still retains non-transient dynamics from isostable coordinates.

3 Results

We perform the 1D and 3D reductions for a set of example model systems and compare the reductions to the full model. We begin by applying the reductions to a forced CGL model (Section 3.1.1) and a forced thalamic neuron (Section 3.1.2). We then turn to applying the reductions to a pair of thalamic neurons (Section 3.2.1) and a pair of mixed model types, where we reciprocally couple a thalamic neuron model to a model of circadian rhythms (Section 3.2.2). For each example, we normalize each oscillator period to 2π by adjusting its natural frequency directly, prior to exploring $n:m$ phase-locking. This choice simplifies our numerical simulations without necessarily losing generality.

3.1 Forcing

We use the same formulation to reduce coupled oscillators but with small changes to the details enabled by forcing. In particular, let ω_Y be the forcing frequency and $G(X, \omega_Y t)$ be the “coupling” function. Then (1) becomes

$$\begin{aligned} \frac{1}{\omega_X} \frac{dX}{dt} &= F_X(X) + \varepsilon G_X(X, \theta_Y), \\ \frac{1}{\omega_Y} \frac{d\theta_Y}{dt} &= 1 + \delta/\omega_Y \end{aligned} \quad (26)$$

where $G_X(X, t)$ is some forcing function, and the heterogeneity parameter δ directly modulates the forcing frequency. The choice to include the heterogeneity term directly in the right-hand side of $d\theta_Y/dt$ is without loss of generality for the following reason. If we take Y in (1) to be some oscillator that forces oscillator X (so $G_Y \equiv 0$), then δ alters the vector fields of each oscillator, generically resulting in a change to their natural frequencies. This relative difference in frequencies can simply be captured by directly modifying the natural frequency of the forcing oscillator ω_Y .

The corresponding phase-isostable reduction for (26) is given by

$$\frac{1}{\omega} \phi' = -\frac{\delta}{\omega_Y} + \varepsilon \sum_{\ell=0}^k \sum_{j=0}^{\ell} \psi^{\ell} \mathcal{H}_Z^{(\ell,j)}(\phi), \quad \frac{1}{\omega} \psi' = \kappa \psi + \varepsilon \sum_{\ell=0}^k \sum_{j=0}^{\ell} \psi^{\ell} \mathcal{H}_I^{(\ell,j)}(\phi),$$

where

$$\begin{aligned} \mathcal{H}_Z^{(\ell,j)}(\xi) &= \frac{1}{2\pi m} \int_0^{2\pi m} Z^{(j)}(\xi + \omega s) \cdot K^{(\ell-j)}(\xi + \omega s, s) ds, \\ \mathcal{H}_I^{(\ell,j)}(\xi) &= \frac{1}{2\pi m} \int_0^{2\pi m} I^{(j)}(\xi + \omega s) \cdot K^{(\ell-j)}(\xi + \omega s, s) ds, \end{aligned}$$

or more compactly,

$$\frac{1}{\omega}\phi' = -\frac{\delta}{\omega_Y} + \varepsilon \sum_{\ell=0}^k \psi^\ell \mathcal{H}_Z^{(\ell)}(\phi), \quad \frac{1}{\omega}\psi' = \kappa\psi + \varepsilon \sum_{\ell=0}^k \psi^\ell \mathcal{H}_I^{(\ell)}(\phi), \quad (27)$$

where

$$\mathcal{H}_Z^{(\ell)}(\xi) = \sum_{j=0}^{\ell} \mathcal{H}_Z^{(\ell,j)}(\xi), \quad \mathcal{H}_I^{(\ell)}(\xi) = \sum_{j=0}^{\ell} \mathcal{H}_I^{(\ell,j)}(\xi).$$

We have implicitly used the same assumptions from the coupling case that there is a reasonable separation of timescales between $\hat{\theta}_X$ ($\hat{\theta}_Y$) and s . A scalar version of (27) is straightforward to obtain by integrating the isostable expansions as in Section 2.2.1, using the ‘‘coupling’’ function without the additive heterogeneity parameter b .

Remark 4. *Several observations follow directly from (27).*

- *Linear changes to the forcing frequency ω_Y correspond to linear, vertical shifts in the \mathcal{H} -functions.*
- *For phase-locked states to exist, we look for ε^* , δ^* , and (ϕ_0, ψ_0) such that*

$$0 = -\frac{\delta^*}{\omega_f} + \varepsilon^* \sum_{\ell=0}^k \psi_0^\ell \mathcal{H}_Z^{(\ell)}(\phi_0), \quad 0 = \kappa\psi_0 + \varepsilon^* \sum_{\ell=0}^k \psi_0^\ell \mathcal{H}_I^{(\ell)}(\phi_0).$$

Thus, the problem of finding fixed points for a general strongly forced system is equivalent to finding intersections of nullclines of a two-dimensional system.

- *Stability of phase-locked states may be found by numerically computing the Jacobian and its eigenvalues at a given fixed point in (27).*
- *If the oscillator is strongly attracting, or equivalently, if κ is large relative to small ε , then the ψ equation may be discarded and only expansions in \mathcal{Z} are necessary.*
- *The existence of higher frequency-locked states depends on the choice of forcing function. In particular, we use forcing functions with more than one Fourier frequency, e.g., we avoid using forcing functions such as $\sin(\omega_Y t)$, because sinusoidal functions generally yield 1:m phase-locking [7].*
- *If the forcing function only depends on time, i.e., $G(X, \omega_f t) \equiv G(\omega_f t)$, then the calculation of $\mathcal{H}_Z^{\ell,j}$ ($\mathcal{H}_I^{\ell,j}$) terms simplify to the cross-correlations,*

$$\mathcal{H}_Z^{\ell,j}(\xi) = \mathcal{H}_Z^{(\ell)}(\xi) = \frac{1}{2\pi m} \int_0^{2\pi m} Z^{(\ell)}(\xi + \omega s) \cdot K^{(0)}(s) ds.$$

In this case, some additional observations follow:

- *If $Z^{(\ell)}$ has zero mean, then the autocorrelation above will also have zero mean for all ℓ independent of the choice of $K^{(0)}$ (this fact is straightforward to confirm by observing the constant Fourier coefficient).*
- *If $G(X, \omega_f t) = D \sin(\omega_f j t)$ or $G(X, \omega_f t) = D \cos(\omega_f j t)$ for some $D \in \mathbb{R}^n$ and $j \in \mathbb{Z}$, The autocorrelation will return a function with a Fourier mode of frequency j [7].*
- *If the forcing function is constant and $Z^{(\ell)}$ has zero mean, then the cross-correlation will return the zero function. Thus, some systems are immune to shifts in the forcing function, at least according to first-order averaging.*

There are no particular restrictions on the choice of forcing function besides sufficient smoothness and periodicity, so we use a periodized Gaussian to ensure that there are enough nontrivial Fourier modes. We define the periodized forcing function as

$$p(\omega_Y t) = \sum_{i=-\infty}^{\infty} \exp\left(-(\omega_Y t/\sigma)^2\right).$$

We numerically implement this function by truncating the infinite sum (e.g., only considering indices i such that $|i| \leq 10$) and taking the input modulo 2π . For simplicity, we assume a forcing function with zero mean and no dependence on state variables, but these choices are not necessary to utilize the 3D reduction or the proposed 1D reduction. The forcing function used throughout this section is given by,

$$G(X, \omega_Y t) \equiv G(\omega_Y t) = p(\omega_Y t) - \bar{p}, \quad (28)$$

where G acts on the first variable and \bar{p} is the mean of p on $[0, 2\pi/\omega_Y)$. A plot of the forcing function is shown in Figure 1B.

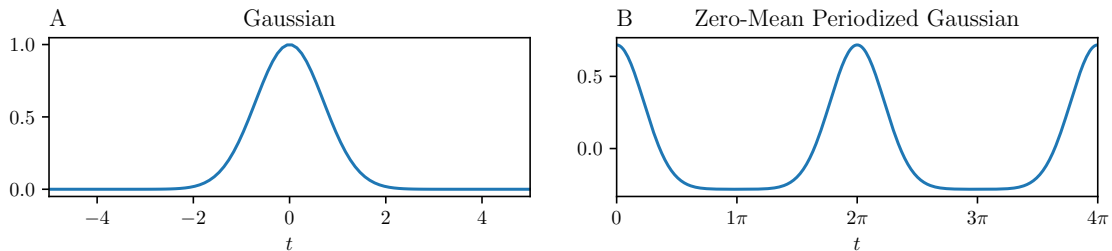


Figure 1: The forcing function. A: The original, unnormalized Gaussian with $\sigma = 1$. B: the periodized Gaussian with zero mean in time.

3.1.1 Complex Ginzburg-Landau Model

The **full model** for this example is a planar version of the complex Ginzburg-Landau (CGL) model [38, 28, 31]:

$$\begin{aligned} \frac{1}{\omega_X} \frac{dX}{dt} &= F_{\text{CGL}}(X) + \varepsilon[-G(\theta_Y), 0]^\top, \\ \frac{1}{\omega_Y} \frac{d\theta_Y}{dt} &= 1 + \delta/\omega_Y, \end{aligned} \quad (29)$$

where $X = [x, y]^\top$,

$$F_{\text{CGL}}(X) = \begin{pmatrix} \sigma x(1 - R^2) - y(1 + \rho(R^2 - 1)) \\ \sigma y(1 - R^2) + x(1 + \rho(R^2 - 1)) \end{pmatrix},$$

$R = \sqrt{x^2 + y^2}$, $\sigma = 0.8$, and $\rho = 0.12$. The Floquet exponent of the isolated limit cycle (at $\varepsilon = 0$) is $\kappa_X \approx -0.16$, making it weakly attracting enough to suitably test the proposed method.

We use a reduction to fourth order in ψ for the 3D reduction, and to the same order in ε for the 1D reduction. There is no special consideration in the choice of order, but using the same order for ψ and ε allows us to compare differences in accuracy between

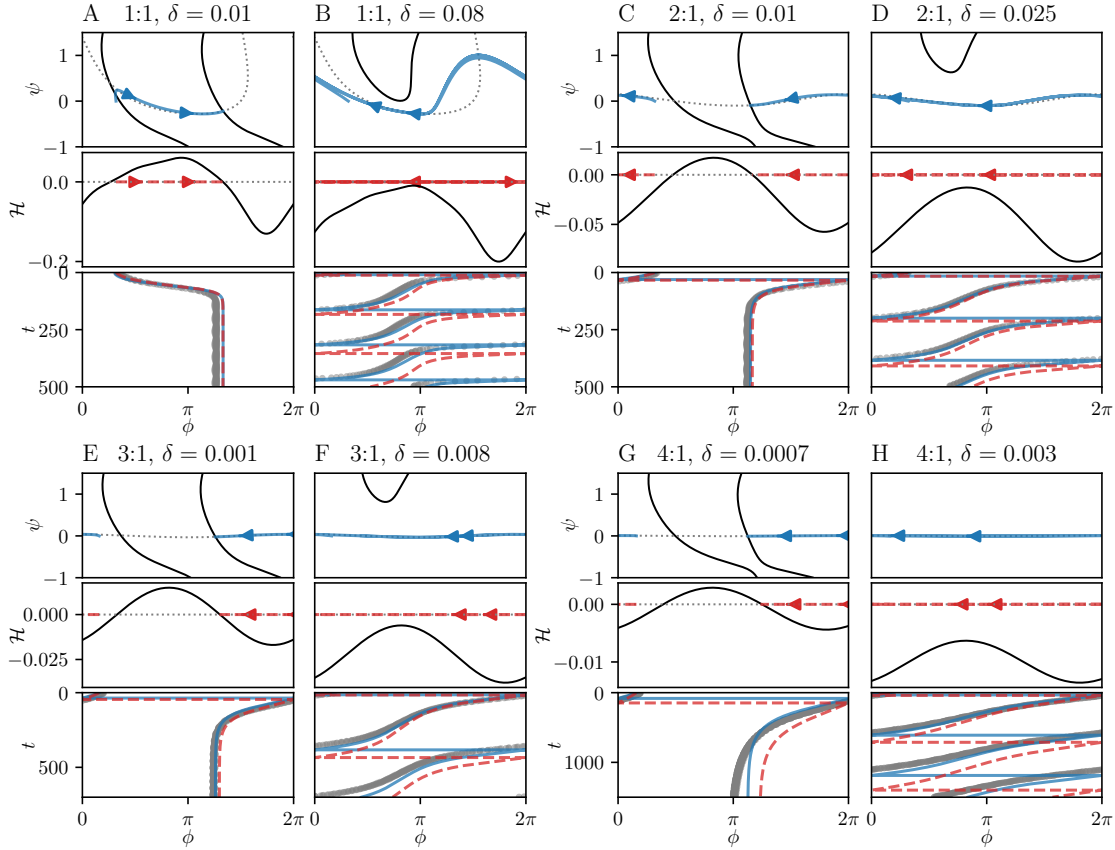


Figure 2: Frequency-locking and drift in a forced CGL model. All panels use the same horizontal axis, $\phi \in [0, 2\pi)$. Each label (A–H) corresponds to particular values of ε and δ , and each labeled panel has three sub-panels, top, middle, and bottom. Each top panel shows the 3D reduction (blue) superimposed on the nullclines (black solid and gray dashed curves). The vertical axis is the averaged isostable coordinate, and the horizontal axis is the averaged phase difference. Each middle panel shows a solution (red) of the 1D reduction superimposed on a plot of its right-hand side (black), with a dashed gray line denoting a height of zero. Each bottom panel shows a plot of the solution of all three model types over time (2D (blue), 1D (red dashed), and full (gray)). A: 1:1 phase-locking for $\varepsilon = 0.2$ and a forcing frequency of $\omega_\gamma + \delta = 1.01$. A, top: The solution of the 3D reduction (blue) with initial condition $(\phi(0), \psi(0)) = (1, 0)$. A, middle: The solution of the 1D reduction (red dashed) with initial condition $\phi(0) = 1$. A, bottom: Phase difference in the full model, 3D reduction, and 1D reduction. Panel 2B shows the same types of plots as in Panel A, but for a forcing frequency of $\omega_\gamma + \delta = 1.08$ with $\varepsilon = 0.2$. The remaining panel pairs (C,D), (E,F), and (G,H) show the same information as Panels (A,B), but for 2:1, 3:1, and 4:1, forcing, respectively, using $\varepsilon = 0.1$ for the coupling strength. Panel pair (C,D) uses the same initial conditions as (A, B), while Panel pairs (E,F) and (G,H) use the initial conditions $(\phi(0), \psi(0)) = (0.5, 0)$ for the 3D reduction and $\phi(0) = 0.5$ for the 1D reduction. We plot every hundredth point in the full model's phase estimate to reduce lag when loading the figure.

the reductions. In general, we expect the 1D reduction to be less accurate because 1. it ignores potentially important transient dynamics in ψ , and 2. fourth order in ε does not necessarily capture all fourth order dynamics in ψ , because, for example, several terms of order ε^n for $n \geq 2$ are neglected when plugging expansions in powers of ε into ψ^4 and truncating to order $O(\varepsilon^4)$.

Trajectories of the three model types (2D, 1D, and full) for the CGL model are shown in Figure 2. Each label (A–H) corresponds to particular values of ε and δ , where resulting solutions of the 2D reduction (blue), 1D reduction (red), and full model (gray) are shown, using approximately the same initial conditions. The label pairs

(A,B), (C,D), (E,F), and (G,H) each show a transition from phase-locking to phase drift induced by sufficiently increasing the heterogeneity parameter δ . Both 1D and 2D reductions are able to capture this transition.

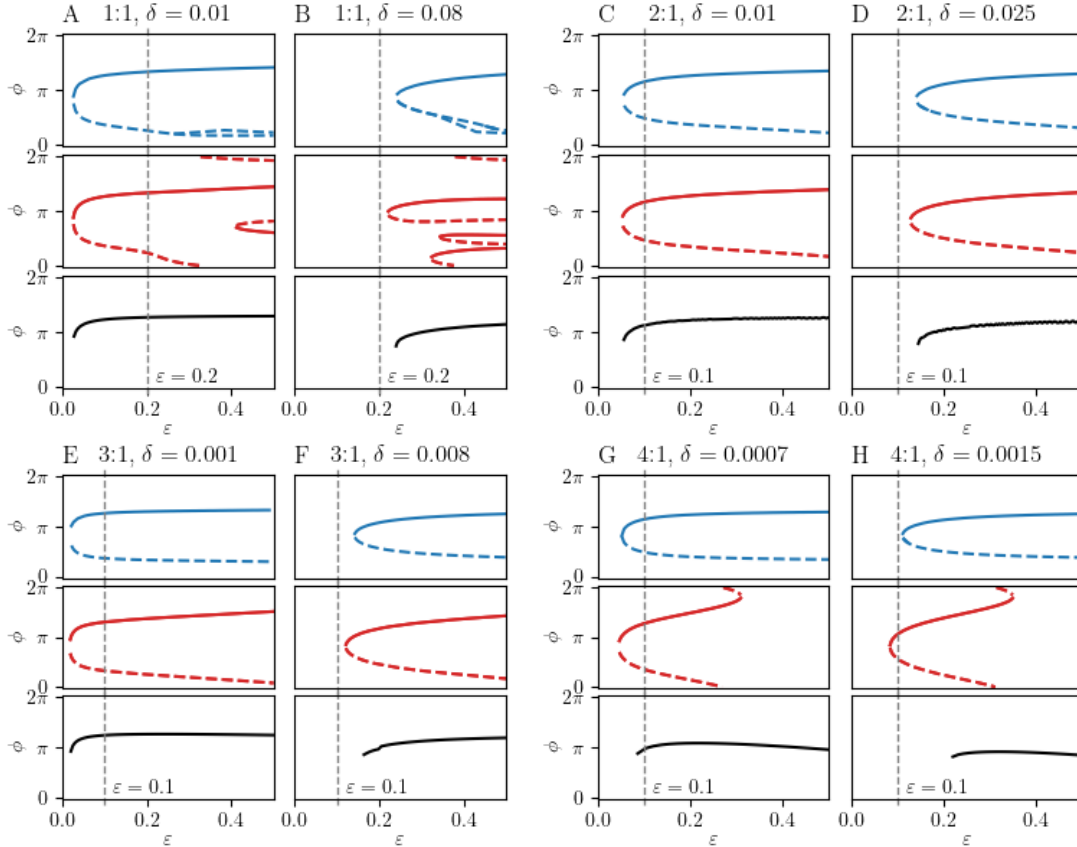


Figure 3: One-parameter bifurcation diagrams of the forced CGL model as a function of coupling strength $\varepsilon \in [0, 0.5]$. Each panel A–H (and each of their sub-panels) corresponds directly to the same system and parameters as panels A–H in Figure 2. In particular, for each panel A–H, the top, middle, and bottom sub-panels correspond to the 2D reduction (blue), 1D reduction (red), and full model (black), respectively. The vertical gray dashed line spanning the top, middle, and bottom sub-panels of each panel A–H correspond to the ε parameter value used in the corresponding panel in Figure 2.

One-parameter bifurcation diagrams of the three model types (2D, 1D, and full) for the CGL model are shown in Figure 3. All panels A–H of this figure correspond to the same panels A–H in Figure 2. The 2D (blue) and 1D (red) reductions capture the same bifurcations leading to the loss of frequency-locked states. Note that the values of δ at which frequency-locking is lost differ by orders of magnitude between 1:1 locking (Figure 2A,B or Figure 3A,B) and 4:1 locking (Figure 2G,H or Figure 3G,H). This observation is consistent with the fact that Fourier coefficients become vanishingly small as $n \rightarrow \infty$ in $n:1$ locking, and that the bandwidth of $n:m$ locking decreases as a function of higher frequencies [7].

Remark 5. *Bifurcation diagrams for the full model and phase-isostable reduction were computed manually using Newton’s method. We iterated the method to find fixed points in phase-locked states for a given ε and δ . If the method successfully converged within a few dozen iterations, the bifurcation parameter ε was incremented by a small amount*

and Newton’s method applied again to search for fixed phase-locked states. This process was repeated until Newton’s method was unable to converge onto a fixed point. This method, while time consuming, was necessary because we were unable to use existing tools such as *XPPAUTO* to compute more precise bifurcation diagrams. For this reason, we have no indicators for specific bifurcations throughout this paper.

Discrepancies between the 2D (blue) and 1D (red) reductions in each of Figures 2 and 3 show that retaining explicit isostable coordinates may be necessary when a greater degree of accuracy is desired for greater values of coupling strengths ε , although the two reductions are often quantitatively and qualitatively similar. Figure 3G,H in particular show how even small differences can lead to qualitatively distinct behaviors for very small δ values. In particular, with higher oscillation frequency relative to the forcing frequency, smaller values of δ can yield phase drift, showing that **even small degrees of heterogeneity can alter the existence of phase-locked states**.

On the note of discrepancies, the bifurcations in phase-locked states appear to differ between the 1D and 2D reductions for greater values of ε , as seen in Panel pairs (A,B) and (G,H) of Figure 3. We have not established the precise reasons for this difference, although the two broad reasons are that 1. the 1D reduction is defined *a priori* as a truncation of ψ , and 2. additional phase difference dynamics that emerge for strong coupling strengths ε that can not be captured by a scalar reduction (e.g., oscillations). While the precise reasons may not be established, we choose to display these discrepancies to highlight potential limitations of the 1D reduction relative to the 2D reduction (and vice-versa, if any).

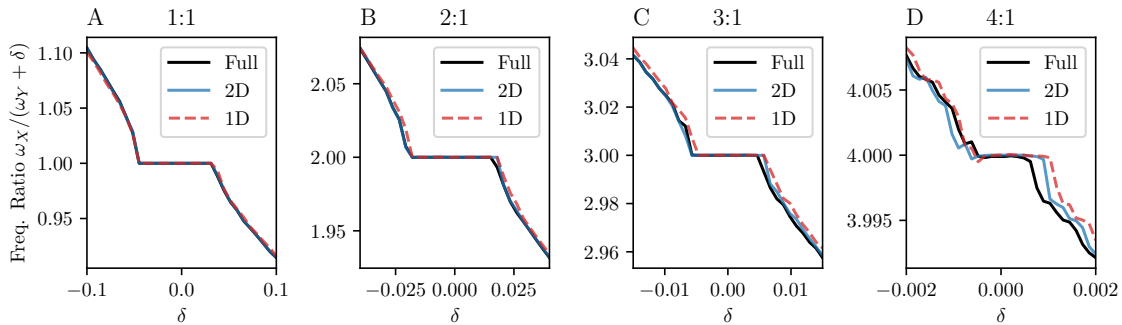


Figure 4: Frequency ratio between the CGL model and its forcing function. Frequencies are obtained by estimating the time elapsed for an oscillation to return to zero phase for each model type (in the full model, zero phase is taken to be the most prominent local maximum of the first coordinate, as is typical for neural models). Parameters are the same as in Figure 2, but with $\varepsilon = 0.1$ for Panels A–C and $\varepsilon = 0.6$ for Panel D.

Frequency ratios of the full and reduced models for varying values of heterogeneity δ are shown in Figure 4. In Panels A–C, both the 1D and 2D reductions accurately reproduce the range of locking frequencies and the phase drift outside the locking regions, at least for the range of δ values considered. As the forcing frequency increases, the range of frequency-locking decreases such that frequency ratios are difficult to obtain numerically at 4:1 locking (Panel D).

Arnold tongues for the 2D (blue) and 1D (red dashed) reductions are shown in Figure 5. The dependence of locking bandwidth on forcing frequency is especially apparent. Again, depending on one’s needs, the 1D reduction could be deemed sufficiently similar to the 2D reduction, although their similarity drops off greatly for even small values of ε at 4:1 locking. We remark briefly that the Arnold tongues of the 2D reduction

Table 1: Parameter values of the nondimensionalized thalamic model (30)

Parameter	E_K	E_{Na}	E_t	E_L	g_L	g_K	g_{Na}	$g_{syn} \equiv \varepsilon$	I_{app}	α	β
Value	-0.9	0.5	0	-0.7	0.05	5	3	0-0.3	0.035	3	2

tend to cut off sooner for increasing values of the coupling strength ε compared to the 1D reduction because we only search for the existence of stable phase-locked states for isostable values in the range $\phi \in [-1, 1]$. Thus, stable fixed points (θ^*, ψ^*) with $|\psi^*| > 1$ are ignored, leading to the occasional premature truncation of an Arnold tongue.

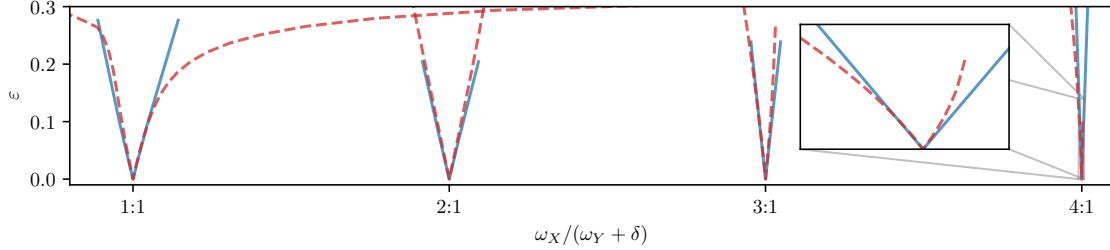


Figure 5: Arnold tongues in the reduced models of the forced CGL model. The vertical axis is the forcing amplitude ε , and the horizontal axis corresponds to the frequency ratio between the CGL model and the forcing function. The 2D reduction (blue) qualitatively matches the 1D reduction (red dashed).

3.1.2 Thalamic Neuron

The **full model** for this example is a nondimensionalized Thalamic model (adapted from [33]),

$$\begin{aligned} \frac{1}{\omega_X} \frac{dX}{dt} &= F_{\text{Thal}}(X) + \varepsilon[-G(\theta_Y), 0, 0]^\top, \\ \frac{1}{\omega_Y} \frac{d\theta_Y}{dt} &= 1 + \delta/\omega_Y, \end{aligned} \quad (30)$$

where $X = [V, h, r]^\top$,

$$F_{\text{Thal}}(X) = \begin{pmatrix} -I_L(V) - I_{Na}(V) - I_K(V) - I_T(V) + I_{app} \\ (h_\infty(V) - h)/\tau_h(V) \\ (r_\infty(V) - r)/\tau_r(V) \end{pmatrix}.$$

The remaining equations are given by

$$\begin{aligned} I_L(V) &= g_L(V - E_L), & I_{Na}(V) &= g_{Na} h m_\infty^3(V)(V - E_{Na}), \\ I_K(V) &= g_K [0.75(1 - h)]^4 (V - E_K), & I_T(V) &= g_T r p_\infty^2(V)(V - E_T), \end{aligned}$$

and

$$\begin{aligned} a_h(V) &= 0.128 \exp(-5.556(V + 0.46)), & b_h(V) &= 4/(1 + \exp(-20(V + 0.23))), \\ m_\infty(V) &= 1/(1 + \exp(-14.29(V + 0.37))), & h_\infty(V) &= 1/(1 + \exp(25(V + 0.41))), \\ r_\infty(V) &= 100/(1 + \exp(25(V + 0.84))), & p_\infty(V) &= 0.01/(1 + \exp(-16.13(V + 0.6))), \\ \tau_h(V) &= 1/(a_h(V) + b_h(V)), & \tau_r(V) &= 28 + \exp(-9.52(V + 0.25)), \\ a_\infty(V) &= 1/(1 + \exp(-125(V + 0.2))). \end{aligned}$$

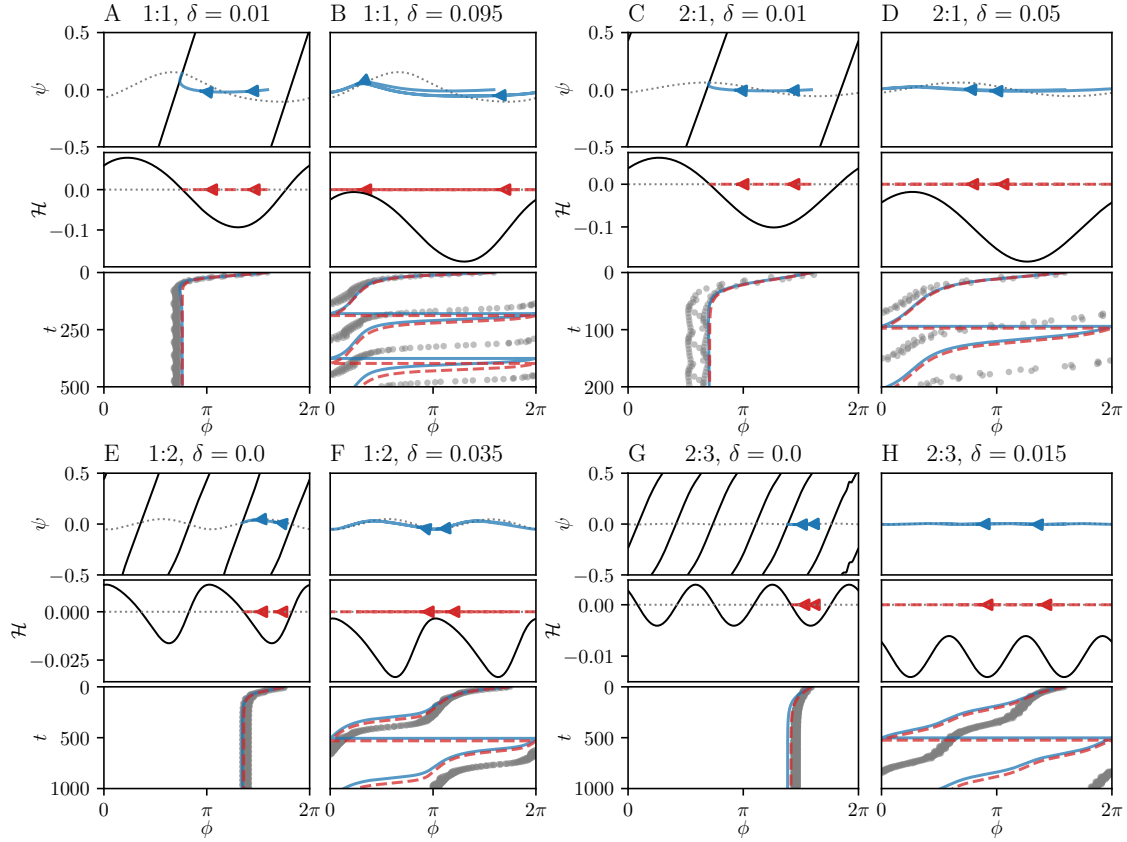


Figure 6: Frequency-locking and drift of a forced thalamic neuron. Each panel shows the same type of information as the corresponding panels in Figure 2. We choose $\varepsilon = 0.05$ for all panels except panel pair (G,H), where $\varepsilon = 0.03$. To reduce lag when loading the figure, only every hundredth point of the full model's phase estimate (gray) is shown.

Nondimensional parameter values are listed in Table 1¹. The Floquet exponent of the isolated limit cycle (at $\varepsilon = 0$) is $\kappa_X \approx -0.024$, making it weakly attracting enough to suitably test the proposed method.

We use a reduction to fourth order in ψ for the 2D reduction, and to the fourth order in ε for the 1D reduction. As in the forced CGL example (Section 3.1.1), there is no special consideration in the choice of order, and we use the same order for ψ and ε to compare what features, if any, are missing in the 1D reduction compared to the 2D reduction and vice-versa.

We fix the forcing strength at $\varepsilon = 0.1$ and observe the existence of frequency-locking in Figure 6 (note that every panel in this figure uses the same horizontal axis). Each panel in this figure shows the same information as the corresponding panels of the forced CGL model in Figure 2. However, we now show a different set of frequency ratios because $n:m$ locking is now possible for $n, m > 1$. In particular, we choose 1:1, 2:1, 1:2, and 2:3 for the purpose of illustration, although other combinations are likely possible.

¹To obtain the original thalamic model, rescale the voltage by multiplying it by 100 mV, and rescale the gating variable r by dividing it by 100 mV. Conductances are scaled using 1 nS. We choose the characteristic scale of 100 mV because it is similar to the potassium reversal potential ($E_K = -90$ mV).

One-parameter bifurcation diagrams of the 2D reduction (blue), 1D reduction (red), and full model (black) are shown in Figure 7. All panels A–H of this figure correspond to the same panels A–H in Figure 6, but with ε varied in the interval $[0, 0.3]$. To help make the correspondence more concrete, consider panel A of Figure 7. The top, middle, and bottom panels are the one-parameter bifurcation diagrams of the 2D (blue), 1D (red), and full models (black), respectively. All horizontal axes share the same ε values in the same interval $[0, 0.3]$. The dashed vertical line across all three sub-panels correspond to the $\varepsilon = 0.05$ value used to plot the trajectories in Figure 6A. Solid curves correspond to stable fixed points and dashed curves correspond to unstable fixed points. Unstable phase-locked states of the full model were unable to be obtained. We use Newton’s method to generate the bifurcation diagrams for the full and 2D reductions as briefly discussed in Remark 5.

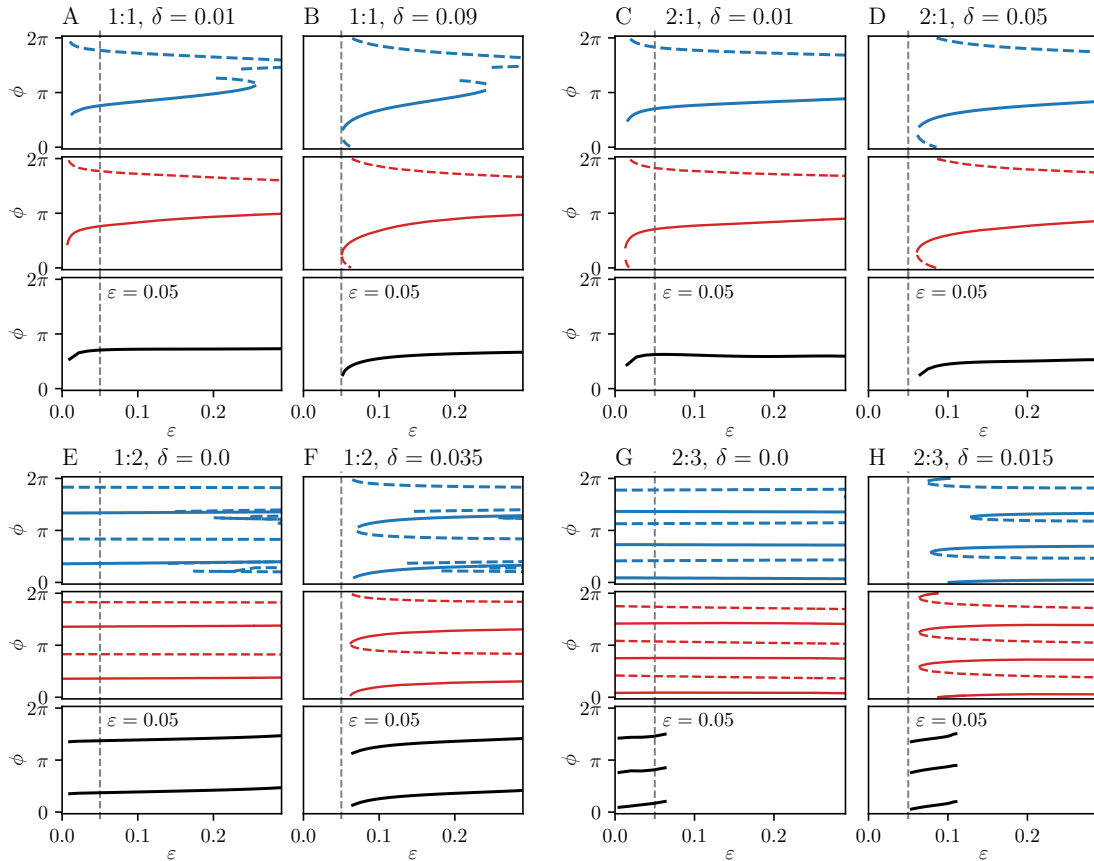


Figure 7: One-parameter bifurcation diagrams of the forced thalamic model as a function of coupling strength ε . Each panel A–H corresponds directly to the same system and parameters as panels A–H in Figure 6. In particular, for each panel A–H, the top, middle, and bottom sub-panels correspond to the 2D reduction (blue), 1D reduction (red), and full model (black), respectively. The vertical gray dashed line spanning the top, middle, and bottom sub-panels of each panel A–H correspond to the ε parameter value used in the corresponding panel in Figure 6. In Panel H, there is a period-doubling bifurcation in the thalamic model near $\varepsilon = 0.05$, but we choose not to analyze this bifurcation further.

Similar to the forced CGL model, we observe similar differences between the 2D (blue) and 1D (red dashed) reductions across the panels. Aside from minor discrepancies, both the 2D and 1D reductions capture qualitative changes to the existence and stability of phase-locked states in the full model. The only exceptions are Panels G

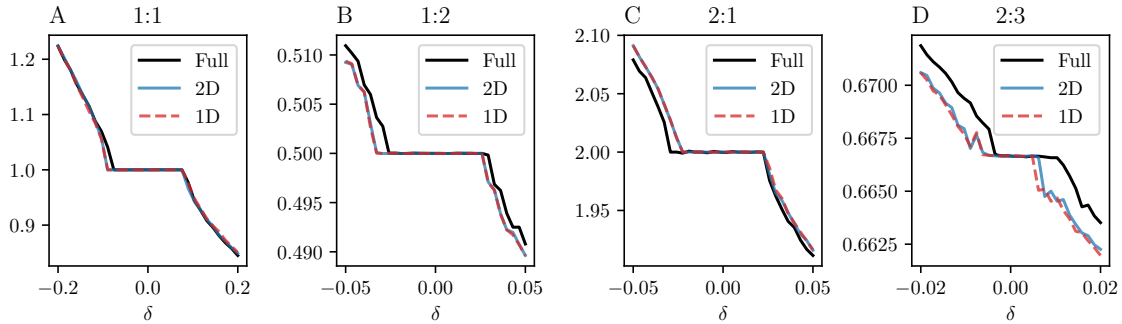


Figure 8: Frequency ratios between the thalamic model and its forcing function. Frequencies are obtained in the same manner as Figure 4. Parameters are the same as in Figure 6, but with $\varepsilon = 0.05$ for Panels A–B and $\varepsilon = 0.03$ for Panels C–D.

and H, where the full model exhibits at least one additional bifurcation (in particular a period-doubling bifurcation) that we do not choose to analyze pursue using the reductions.

We take a closer look at these qualitative differences in Figure 8, where we plot frequency ratios as a function of heterogeneity. Additional context for the existence and non-existence of phase-locked states is shown in the Arnold tongues of the 2D (blue) and 1D (red dashed) reductions in Figure 9. There is strong qualitative agreement between the reductions.

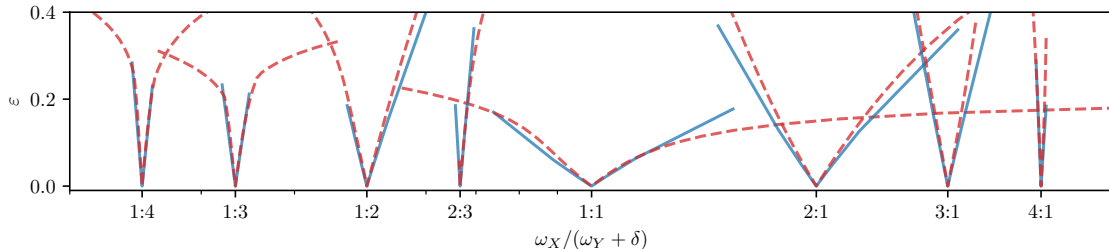


Figure 9: Arnold tongues of the forced thalamic neuron. The vertical axis is the forcing amplitude ε , and the horizontal axis corresponds to the frequency ratio between the thalamic model and the forcing function. The 2D reduction (blue) closely matches the 1D reduction (red dashed). Note that the horizontal axis is on a logarithmic base-10 scale, where 1:1 corresponds to 10^0 .

3.2 Coupling

In this section, we consider a pair of thalamic models (Section 3.2.1), and a thalamic model reciprocally coupled to a different biologically-relevant model of circadian oscillations (Section 3.2.2). We choose not to consider the CGL model because a pair of reciprocally coupled CGL models exhibit no stable $n:m$ phase-locking for $n > 1$ or $m > 1$ due to all its response functions containing only the principal mode.

3.2.1 A Pair of Thalamic Neurons with Heterogeneity

The **full model** for this example is a pair of synaptically coupled thalamic neurons [33]. We use the same vector field as the forced thalamic model (30) and the same parameters (Table 1) with an additional variable (w) representing a chemical synapse:

$$\hat{F}_{\text{Thalamic}}(X) = \begin{pmatrix} F_{\text{Thalamic}}(X) \\ \alpha(1-w)a_{\infty}(V) - \beta w \end{pmatrix},$$

where $X = [V_1, h_1, r_1, w_1]^{\top}$ ($Y = [V_2, h_2, r_2, w_2]^{\top}$). The coupled equations are given by,

$$\begin{aligned} \frac{1}{\omega_X} \frac{dX}{dt} &= \hat{F}_{\text{Thalamic}}(X) + \delta + \varepsilon[G_2(X, Y)]^{\top}, \\ \frac{1}{\omega_Y} \frac{dY}{dt} &= \hat{F}_{\text{Thalamic}}(Y) + \varepsilon[G_2(Y, X)]^{\top}, \end{aligned} \quad (31)$$

where $e \equiv g_{\text{syn}}$ is the synaptic conductance and

$$G_2(X, Y) = [w_2(V_1 - E_{\text{syn}}), 0, 0, 0]^{\top}.$$

In this example, we choose an excitatory synapse with $E_{\text{syn}} = -0.001$.

Remark 6. *Choosing heterogeneity independent of the variables X or Y is a simplification but not necessary. For instance, we may include an additional source of heterogeneity by writing $E_{\text{syn}} = \bar{E}_{\text{syn}} + \delta_i$. The right-hand sides of (31) are then*

$$\begin{aligned} \hat{F}_{\text{Thalamic}}(X) + \delta - \delta_X w_2 + \varepsilon[w_2(V_1 - \bar{E}_{\text{syn}}), 0, 0, 0]^{\top}, \\ \hat{F}_{\text{Thalamic}}(Y) - \delta_Y w_2 + \varepsilon[w_1(V_2 - \bar{E}_{\text{syn}}), 0, 0, 0]^{\top}, \end{aligned}$$

which is a form amenable to the proposed method. In general, we anticipate taking Taylor expansions for heterogeneous parameters in nonlinear terms.

The scalar reduction is capable of reproducing various phase-locked states in the full thalamic model for $n:m$ coupling considered, including 1:1 (Figure 10A,B), 1:2 (Figure 10C,D), 2:1 (Figure 10E,F), and 2:3 (Figure 10G,H). Most behaviors qualitative behaviors between the full model and reductions agree, with the only noticeable discrepancy between the 3D and 1D reductions in Figure 10B, where the 1D reduction captures the emergence of a new phase-locked state at $b = 0.001$ and $\varepsilon = 0.1$, while the 3D reduction does not appear to capture the same bifurcation. Additional phase-locking combinations are possible, but are not shown or were not considered.

The 3D reduction appears to be unable to capture the near-synchronous but non-zero phase-locked state for 1:1 locking (Figure 10B), in contrast to the 1D reduction, which successfully captures this bifurcation as a function of b . We did not thoroughly investigate the cause for this difference, but a possible factor is that our implementation of the 3D model exhibits large transients in the isostable coordinates that lead to integration failures, even with absolute and relative tolerances on the order of 1×10^{-9} and with LSODA, a robust numerical ODE solver. It is also possible that pre-computing averages may help in this case, because our implementation of the 3D reduction computes averaging integrals at each time step.

One-parameter bifurcation diagrams for this example are shown in Figures 11 (1:1), 12 (1:2), and 13 (2:3). In most cases, both 3D (blue) and 1D (red) reductions capture the changes to phase-locked states as a function of ε for various given values of the heterogeneity parameter δ , with the notable exception being the bifurcation diagram for 1:1 locking (Figure 11), where the 3D reduction was unable to capture the emergence of new branches for increasing ε . We use Newton's method to compute the bifurcation diagrams for the 3D reduction and full model (see Remark 5).

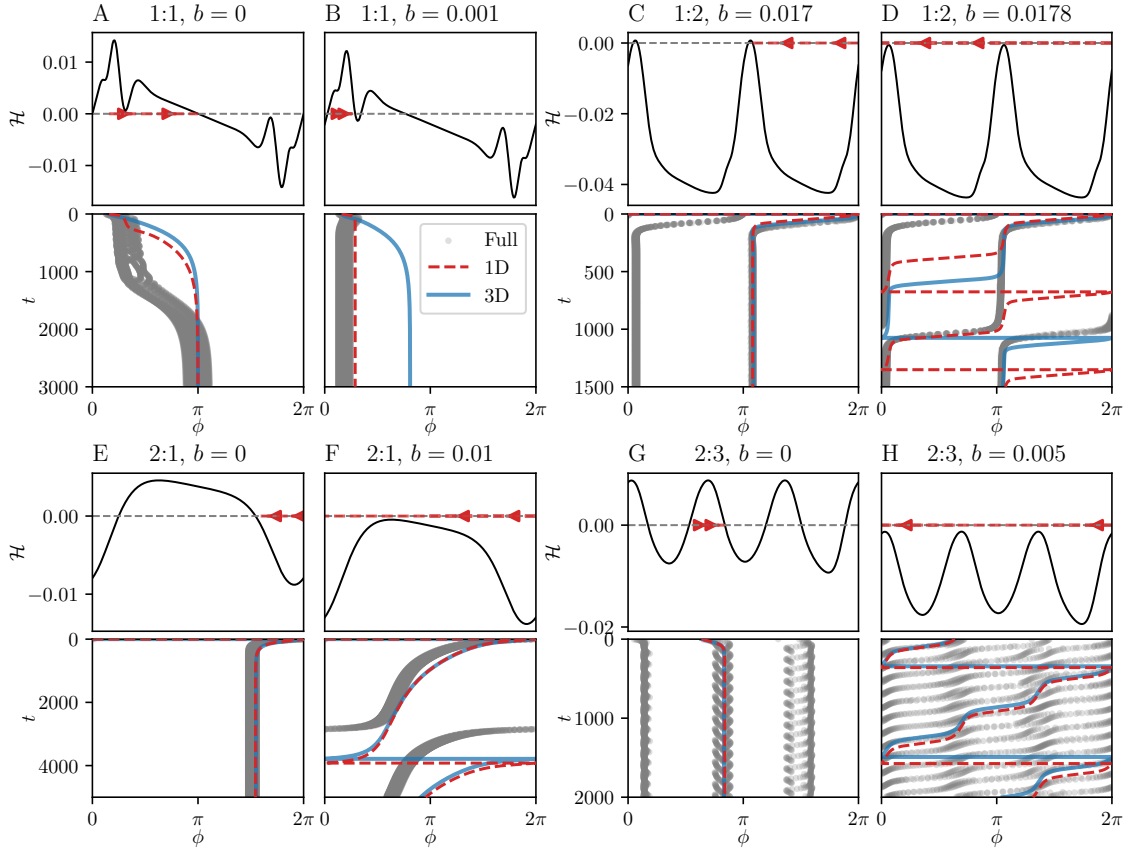


Figure 10: Phase-locking and drift between a pair of coupled thalamic neurons. The coupling strength ε is chosen to be $\varepsilon = 0.1$ for panels (A,B), $\varepsilon = 0.08$ for panels (C,D), $\varepsilon = 0.025$ for panels (E,F), and $\varepsilon = 0.1$ for panels (G,H).

3.2.2 A Pair of Mixed Models with Heterogeneity

The **full model** for this example is a thalamic neuron model reciprocally coupled to a model of circadian oscillations (the Goodwin oscillator, adapted from [12]). The vector fields and coupling functions are as follows:

$$\begin{aligned} \frac{1}{\omega_X} \frac{dX}{dt} &= \hat{F}_{\text{Thalamic}}(X) + \delta + \varepsilon G_X(X, Y), \\ \frac{1}{\omega_Y} \frac{dY}{dt} &= F_{\text{Goodwin}}(Y) + \varepsilon G_Y(X, Y), \end{aligned} \quad (32)$$

where $X = [V_1, h_1, r_1, w_1]^\top$, $Y = [x_2, y_2, z_2, w_2]^\top$, and

$$F_{\text{Goodwin}}(Y) = \begin{pmatrix} \nu_1 \frac{k_1^6}{k_1^6 + z_2^6} - \nu_2 \frac{x_2}{k_2 + x_2} \\ k_3 x_2 - \nu_4 \frac{y_2}{k_4 + y_2} \\ k_5 y_2 - \nu_6 \frac{k_6 + z_2}{k_6 + z_2} \\ k_7 x_2 - \nu_8 \frac{k_8 + c_2}{k_8 + c_2} \end{pmatrix}, \quad G_Y(X, Y) = \begin{pmatrix} \frac{(w_1 + w_2)k}{2k_c} \\ 0 \\ 0 \\ 0 \end{pmatrix}, \quad (33)$$

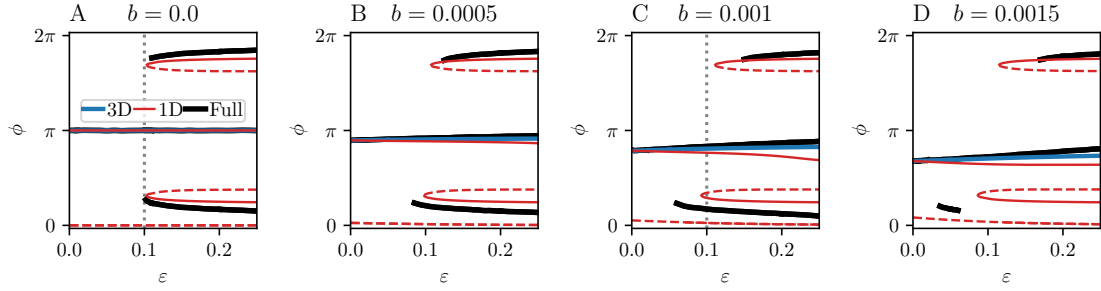


Figure 11: Bifurcation diagrams for 1:1 phase-locking in a pair of thalamic neurons given varying levels of heterogeneity. Vertical dotted lines mark where $\varepsilon = 0.1$, the coupling strength used in Figure 10A,B.

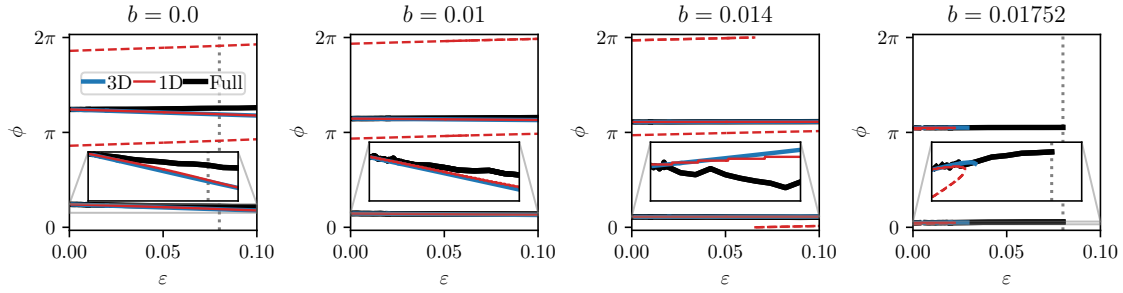


Figure 12: Bifurcation diagrams for 1:2 phase-locking in a pair of thalamic neurons given varying levels of heterogeneity. The inset simply shows that multiple curves overlap. Vertical dotted lines mark where $\varepsilon = 0.08$, the coupling strength used in Figure 10B,C.

The coupling function of the Goodwin oscillator is taken to be the first-order expansion of its original form, $kF/(k_c + kF)$ and $F = (w_1 + w_2)/2$. The Goodwin oscillator has been used to understand spontaneous synchronization of cells in the suprachiasmatic nucleus (SCN) that are responsible for generating circadian rhythms [12]. It exhibits a slowly decaying mode ($\kappa \approx -0.16$ after normalizing the period to 2π), making it well-suited to test the proposed method. Parameter values for the Goodwin oscillator are given in Table 2, and we use the same nondimensional parameters for the Thalamic model in Table 1, with the only changes being the driving current $I_{\text{app}} = 0.085$ and the synaptic reversal potential $E_{\text{syn}} = -0.9$ (i.e., the thalamic neuron is now inhibitory). The vector $Y = [x_2, y_2, z_2, w_2]^T$ represents the mRNA concentration of a clock gene (x_2), the resulting protein (y_2), the active protein or the nuclear form the protein (z_2), and neurotransmitter concentration (w_2), respectively.

This example is loosely motivated by the interaction of SCN neurons with upstream synaptic inputs. The coupling from the Goodwin oscillator to the thalamic model and vice-versa resemble chemical interactions between the populations. While this example is not necessarily biologically realistic, it nevertheless serves to verify that the proposed method provides an accurate and efficient low-dimensional approximation of $n:m$ phase-locked states of two non-planar heterogeneous oscillators. No special consideration was taken when choosing these models except that at least one model has a slowly decaying

Table 2: Parameter values of the Goodwin oscillator (33). Other parameters are $v_8 = k_1 = k_2 = k_4 = k_6 = k_8 = 1$.

Parameter	v_1	v_2	v_4	v_6	k_3	k_5	k_7	K	K_c
Value	0.84	0.42	0.35	0.35	0.7	0.7	0.35	0.5	1

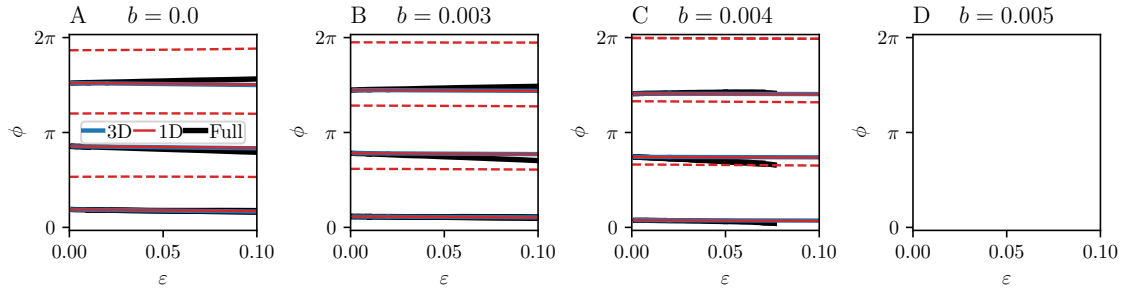


Figure 13: Bifurcation diagrams for 2:3 phase-locking in a pair of thalamic neurons given varying levels of heterogeneity. Phase-locked states disappear through a saddle-node bifurcation in δ , but remain relatively unaffected by the coupling strength ε .

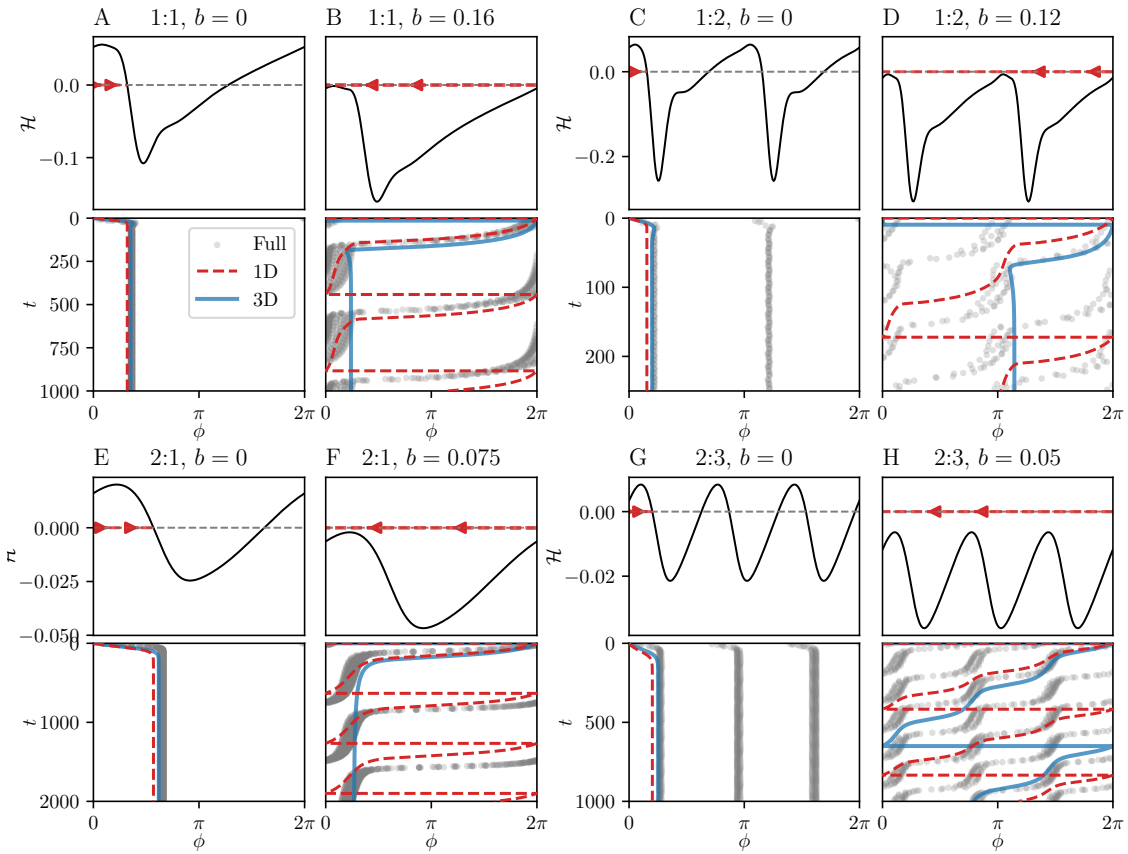


Figure 14: Phase-locking and drift between reciprocally coupled non-identical oscillators. The coupling strength ε is chosen to be $\varepsilon = 0.06$ for panels (A,B), $\varepsilon = 0.1$ for panels (C,D), $\varepsilon = 0.05$ for panels (E,F), and $\varepsilon = 0.05$ for panels (G,H).

Floquet mode (note, however, that it is not necessary for both oscillators to have slowly decaying modes).

A set of example parameter values and trajectories of the 3D reduction (blue), 1D reduction (red dashed), and full model (gray) are shown in Figure 14. The 1D reduction provides an easily-interpretable explanation for the bifurcations that exist in the phase-locked states of the full model.

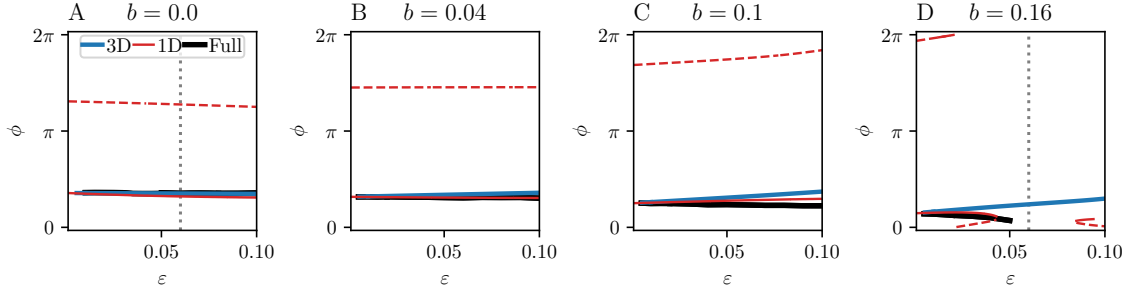


Figure 15: Bifurcation diagrams for 1:1 phase-locking in a pair of mixed models given varying levels of heterogeneity. Vertical dotted lines mark where $\varepsilon = 0.06$, the coupling strength used in Figure 14A,B.

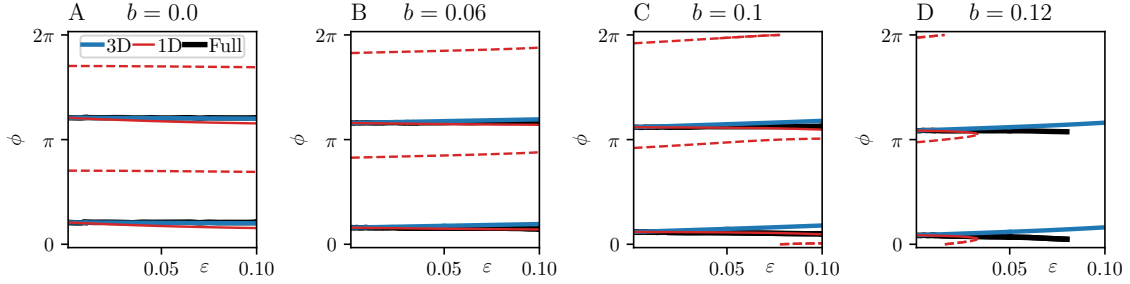


Figure 16: Bifurcation diagrams for 1:2 phase-locking in a pair of mixed models given varying levels of heterogeneity.

One-parameter bifurcation diagrams for this example are shown in Figures 15 for 1:1 locking, 16 for 1:2 locking, and 17 for 2:3 locking. In all cases, both 3D (blue) and 1D (red) reductions capture the changes to phase-locked states as a function of ε for various given values of the heterogeneity parameter b . We use Newton's method to compute the bifurcation diagrams for the 3D reduction and full model (see Remark 5).

In Figures 15 and 16, we find that the 1D reduction (red) faithfully captures the loss of a fixed point as a function of ε for sufficiently large heterogeneity b , while the 3D reduction does not always capture this loss (see panels B, D, and F of each figure). We did not closely investigate the reason for this discrepancy between the 1D and 3D reductions, but it likely stems from small numerical errors in our implementation.

Figure 17 shows that there is some discrepancy between the reductions' ability to capture the loss of phase-locked states as a function of heterogeneity b . However, we refer back to the trajectories of the 1D and 3D reductions in in Figure 14G,H, which closely resemble those of the full model. We thus claim that bifurcations are correctly captured by the reductions, even if the bifurcations do not occur at the exact same value of b between the reductions and the full model.

4 Discussion

We have demonstrated that the proposed 1D reduction captures the same qualitative dynamics and bifurcations of the corresponding full model for values of the forcing or coupling strength ε beyond the weak regime and for nonzero values of heterogeneity δ (or b) for various combinations of $n:m$ coupling. In the case of forcing, the 1D reduction and 3D reduction perform almost as well as each other for a wide range of forcing strengths ε and various alterations to the forcing frequency by the parameter δ . In the

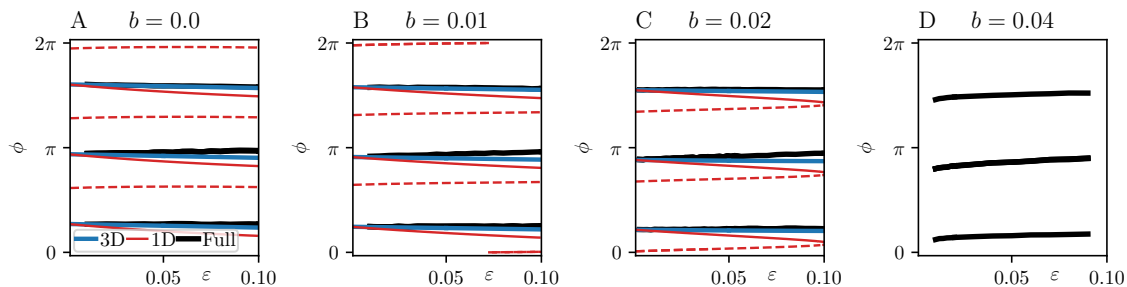


Figure 17: Bifurcation diagrams for 2:3 phase-locking in a pair of mixed models given varying levels of heterogeneity.

case of coupling, the 1D reduction performs well both for identical coupled models with heterogeneity, and for dissimilar coupled models with heterogeneity.

We first highlight some important observations. Across virtually all results, the magnitude of heterogeneity b is very small, often much smaller than the coupling strength ε , before yielding significant changes to the existence and stability of phase-locked states. This observation suggests that methods like H/K theory, that show the existence and stability of fixed points for even very strong coupling, may ultimately find limited use in biologically realistic contexts, where heterogeneity is an important (if not necessary) part of function.

Because we often chose heterogeneity to be extremely small, most observed changes to the existence and stability of fixed points as a function of the heterogeneity parameter b are likely linear, with little contribution from higher-order terms in b . Just how much higher-order heterogeneity terms contribute to altering phase-locked states will be worth investigating in future work. Finding analytically tractable examples with nontrivial Fourier modes will be important to this end.

4.1 Limitations

4.1.1 Assumptions

The proposed 1D reduction relies on having a reasonable separation of timescales between the phase difference dynamics and the limit cycle period, so that first-order averaging can be used to turn non-autonomous equations into relatively tractable autonomous equations. However, the *a priori* limitation of this assumption has not been clearly established in this context. For now, we choose to truncate the ε -expansions at the lowest order where desired qualitative behaviors are captured, where additional terms do not improve performance.

Our method also assumes that the inter-spike-intervals (ISIs) are constant as a function of coupling strength ε , but ISIs tend to become non-equal as coupling strength increases (data not shown). While the scalar reduction manages to perform reasonably well assuming ISIs are equal, allowing non-equal ISIs as part of the assumption could help improve the performance of the method.

4.1.2 Numerics

The proposed 1D reduction is vulnerable to multiple sources of error that can be difficult to track down. These sources include the mesh size of the response functions and the precomputed isostable expansion functions p_i and \mathcal{H} functions, the choice of truncation in ε , and the decision to use first-order averaging. While we made sure to

use sufficiently fine meshes for this work, determining a sufficiently accurate mesh can be time consuming, depending on the underlying response functions. In particular, the higher the Nyquist frequency, the finer the mesh is required to be, and the more time consuming the p_i are to compute. This calculation, however, is a one-time cost for a given ε and δ .

If one wishes to consider large numbers of oscillators, it is clear that using the 3D reduction is far more beneficial. An excellent example involving 200 oscillators and the corresponding version of the 3D reduction (truncated to first order in ψ) can be found in [26]. Here, there is no costly step required to precompute the p_i functions, and despite the increase in dimension for each oscillator, analytical calculations are still possible. Using the scalar reduction, it is possible to consider networks of 3 oscillators (see, e.g., [31]), but it becomes prohibitively costly to precompute the p_i functions for even just 4 oscillators.

4.1.3 Qualitative Dynamics and Bifurcations

While the 1D reduction captures saddle-node bifurcations in phase-locked states, it is by nature unable to capture Hopf bifurcations in phase-locked states for a pair of oscillators, which appears to occur in the phase difference of the thalamic model for sufficiently large ε (data not shown). The scalar model also cannot capture transient oscillations toward phase-locked states that happen to be stable foci (although it can capture the existence and asymptotic stability of a stable focus). Note, however, that for three or more oscillators, the scalar model can capture Hopf bifurcations in the phase difference dynamics as demonstrated in [31].

4.2 Utility of the Proposed Method

Despite the limitations outlined above, the proposed 1D reduction retains significant utility. Multiple authors have already developed and demonstrated scalar reductions well beyond the weak coupling regime using this type of scalar reduction [38, 28, 31, 22]. While there are existing works on scalar reductions with heterogeneity [22], this paper establishes a natural extension to n dimensional systems. We have also made the notation for heterogeneity more concrete and considered multiple coupling examples that are more biologically realistic. Indeed, the proposed formulation for heterogeneity is not just restricted to the case of $N = 2$ oscillators as in [22]. A generalization of this formation to $N \geq 2$ and n -dimensional oscillators is discussed in [31].

There is also practical utility beyond the formulation. The 1D reduction, while potentially cumbersome to compute initially, is extremely efficient to integrate numerically, because the integrator only references an interpolating function for each $\mathcal{H}_i^{(\ell)}$ function. Integrating the 1D model often takes orders of magnitude less time to integrate than the full model and also outperforms the 3D reduction.

As another potentially practical application, the results may be used to introduce more realistic forms of coupling functions to idealized models such as the Kuramoto model. The classic Kuramoto model only uses a pure sine function to describe coupling, but the proposed method may be used to include additional sinusoidal terms that approximate the Fourier expansion of more biologically realistic coupling functions. This idea may be applied naturally beyond the Kuramoto model, e.g., to the higher-order reduction of the Haken-Kelso-Bunz (HKB) equation in [23], which considers the lowest-order Fourier coefficients of the \mathcal{H} -functions of the proposed method. Additional Fourier modes may be computed and added as needed using our method.

We publicly share our numerical methods under an open-source license on [29].

A Taylor Expansions

To expand the coupling functions G_i in powers of ε , we use the Floquet eigenfunction approximation ($g_i^{(k)}$) for each oscillator,

$$\begin{aligned}\Delta X &\approx \psi_X g_X^{(1)}(\theta_X) + \psi_X^2 g_X^{(2)}(\theta_X) + \dots, \\ \Delta Y &\approx \psi_Y g_Y^{(1)}(\theta_Y) + \psi_Y^2 g_Y^{(2)}(\theta_Y) + \dots,\end{aligned}\tag{34}$$

where $\Delta X \equiv X(t) - X_0(\theta_X(t))$ ($\Delta Y \equiv Y(t) - Y_0(\theta_Y(t))$) is the difference between the limit cycle solution X_0 (Y_0) and an arbitrary trajectory $X(t)$ ($Y(t)$) in the basin of attraction. We focus on G_X without loss of generality because the calculations are identical for G_Y , \hat{G}_i , and J_i .

We view the coupling function as the map $G_X : \mathbb{R}^{n_X+n_Y} \rightarrow \mathbb{R}^{n_X}$, where

$$\begin{aligned}G_X(\Xi) &= [G_{X,1}(\Xi), G_{X,2}(\Xi), \dots, G_{X,n_X}(\Xi)]^\top \in \mathbb{R}^{n_X}, \\ G_{X,m} : \mathbb{R}^{n_X+n_Y} &\rightarrow \mathbb{R}, \quad m = 1, 2, \dots, n_X,\end{aligned}$$

and $\Xi = [X^\top, Y^\top]^\top \in \mathbb{R}^{n_X+n_Y}$ is an $(n_X + n_Y) \times 1$ column vector. To make the expansion explicit, we write $\Xi = \Lambda + \Delta\Xi$, where

$$\begin{aligned}\Lambda &= [X_0(\theta_X)^\top, Y_0(\theta_Y)^\top]^\top \in \mathbb{R}^{n_X+n_Y}, \\ \Delta\Xi &= [\Delta X^\top, \Delta Y^\top]^\top \in \mathbb{R}^{n_X+n_Y},\end{aligned}$$

so both are $(n_X + n_Y) \times 1$ column vectors. We now use the “vec” operator from [20, 37] to obtain the multivariate Taylor expansion of $G_{X,m}$ for each $m = 1, 2, \dots, n_X$:

$$G_{X,m}(\Lambda + \Delta\Xi) = G_{X,m}(\Lambda) + G_{X,m}^{(1)}(\Lambda)\Delta\Xi + \sum_{k=2}^{\infty} \frac{1}{k!} \left[\otimes^k \Delta\Xi^\top \right] \text{vec} \left(G_{X,m}^{(k)}(\Lambda) \right), \tag{35}$$

where, temporarily treating Λ as a vector of dummy variables,

$$G_{X,m}^{(k)}(\Lambda) = \frac{\partial \text{vec} \left(G_{X,m}^{(k-1)}(\Lambda) \right)}{\partial \Lambda^\top} \in \mathbb{R}^{(n_X+n_Y)^{(k-1)} \times (n_X+n_Y)}. \tag{36}$$

The vec operator simply reshapes a matrix by stacking its columns, which allows us to avoid calculating high-dimensional tensors. For example, if an $n \times m$ matrix A has columns a_i for $i = 1, \dots, n$ for $a_i \in \mathbb{R}^m$, then $\text{vec}(A)$ is the $mn \times 1$ column vector $(a_1^\top, a_2^\top, \dots, a_n^\top)^\top$. If A is a Jacobian matrix, taking partial derivatives yields a tensor, whereas taking partials of $\text{vec}(A)$ yields a matrix.

We replace $\Delta\Xi$ in (35) with the Floquet eigenfunction expansions (34). Here, it is possible to write the expansion of G_X in terms of ψ_i :

$$\begin{aligned}G_X(\theta_X, \theta_Y, \psi_Y) &= \bar{K}_X^{(0)}(\theta_X, \theta_Y) + \psi_X \bar{K}_X^{(1)}(\theta_X, \theta_Y) + \psi_X^2 \bar{K}_X^{(2)}(\theta_X, \theta_Y) \\ &\quad + \psi_X^3 \bar{K}_X^{(3)}(\theta_X, \theta_Y) + \dots.\end{aligned}\tag{37}$$

Each $\bar{K}_X^{(\ell)}$ function contains terms that depend only on θ_X, θ_Y . We may go a step further and replace each ψ_i with its expansion (11), and collect the expansion in powers of ε . The notation becomes cumbersome, so we summarize this step by writing

$$\begin{aligned}G_X(\theta_X, \psi_X, \theta_Y, \psi_Y) &= K_X^{(0)}(\theta_X, \theta_Y) + \varepsilon K_X^{(1)}\left(\theta_X, \theta_Y, p_X^{(1)}, p_Y^{(1)}\right) \\ &\quad + \varepsilon^2 K_X^{(2)}\left(\theta_X, \theta_Y, p_X^{(1)}, p_X^{(2)}, p_Y^{(1)}, p_Y^{(2)}\right) \\ &\quad + \varepsilon^3 K_X^{(3)}\left(\theta_X, \theta_Y, p_X^{(1)}, p_X^{(2)}, p_X^{(3)}, p_Y^{(1)}, p_Y^{(2)}, p_Y^{(3)}\right) \\ &\quad + \dots.\end{aligned}$$

Each $K_X^{(\ell)}$ function contains the Floquet eigenfunctions and the partials of G_X . It is straightforward to verify using a symbolic package that the function $K_X^{(\ell)}$ only depends on terms $p_X^{(\ell)}, p_Y^{(\ell)}$ for $\ell \leq k$.

References

- [1] Sabina Adhikari, Juan G Restrepo, and Per Sebastian Skardal. Synchronization of phase oscillators on complex hypergraphs. *Chaos: An Interdisciplinary Journal of Nonlinear Science*, 33(3), 2023.
- [2] Aditya Bhaskar, B Shayak, Alan T Zehnder, and Richard H Rand. Integer ratio self-synchronization in pairs of limit cycle oscillators. In *International Design Engineering Technical Conferences and Computers and Information in Engineering Conference*, volume 85482, page V011T11A010. American Society of Mechanical Engineers, 2021.
- [3] Robert J Butera Jr, John Rinzel, and Jeffrey C Smith. Models of respiratory rhythm generation in the pre-Bötzinger complex. ii. populations of coupled pacemaker neurons. *J. Neurophysiol.*, 82(1):398–415, 1999.
- [4] Carmen C Canavier, Fatma Gurel Kazanci, and Astrid A Prinz. Phase resetting curves allow for simple and accurate prediction of robust N:1 phase locking for strongly coupled neural oscillators. *Biophys. J.*, 97(1):59–73, 2009.
- [5] JY Chen, KW Wong, HY Zheng, and JW Shuai. Phase signal coupling induced n: m phase synchronization in drive-response oscillators. *Physical Review E*, 63(3):036214, 2001.
- [6] Irving R Epstein and John A Pojman. *An introduction to nonlinear chemical dynamics: oscillations, waves, patterns, and chaos*. Oxford University Press, 1998.
- [7] G. Bard Ermentrout. n:m phase-locking of weakly coupled oscillators. *J. Math. Biol.*, 12(3):327–342, 1981.
- [8] G. Bard Ermentrout and David H. Terman. *Mathematical foundations of neuroscience*, volume 35 of *Interdisciplinary Applied Mathematics*. Springer, New York, 2010.
- [9] Leon Glass and Rafael Perez. Fine structure of phase locking. *Physical Review Letters*, 48(26):1772, 1982.
- [10] Eli E Goldwyn and Alan Hastings. Small heterogeneity has large effects on synchronization of ecological oscillators. *Bulletin of Mathematical Biology*, 71:130–144, 2009.
- [11] Martin Golubitsky and Ian Stewart. *The symmetry perspective: from equilibrium to chaos in phase space and physical space*, volume 200. Springer Science & Business Media, 2003.
- [12] Didier Gonze, Samuel Bernard, Christian Waltermann, Achim Kramer, and Hanspeter Herzel. Spontaneous synchronization of coupled circadian oscillators. *Biophysical journal*, 89(1):120–129, 2005.
- [13] Viktor Horváth, Daniel Jackson Kutner, Manhao Danny Zeng, and Irving R. Epstein. Phase-frequency model of strongly pulse-coupled Belousov-Zhabotinsky oscillators. *Chaos: An Interdisciplinary Journal of Nonlinear Science*, 29(2):023128, 02 2019.

- [14] Ian Hunter, Michael M. Norton, Bolun Chen, Chris Simonetti, Maria Eleni Moustaka, Jonathan Touboul, and Seth Fraden. Pattern formation in a four-ring reaction-diffusion network with heterogeneity. *Phys. Rev. E*, 105:024310, Feb 2022.
- [15] Eugene M. Izhikevich. *Dynamical systems in neuroscience: the geometry of excitability and bursting*. Computational Neuroscience. MIT Press, Cambridge, MA, 2007.
- [16] Y. Kuramoto. *Chemical oscillations, waves, and turbulence*, volume 19 of *Springer Series in Synergetics*. Springer-Verlag, Berlin, 1984.
- [17] Johannes Lengler, Florian Jug, and Angelika Steger. Reliable neuronal systems: the importance of heterogeneity. *PloS one*, 8(12):e80694, 2013.
- [18] J. Llibre, D. D. Novaes, and M. A. Teixeira. Higher order averaging theory for finding periodic solutions via Brouwer degree. *Nonlinearity*, 27(3):563–583, 2014.
- [19] M. Maggia, S. A. Eisa, and H. E. Taha. On higher-order averaging of time-periodic systems: reconciliation of two averaging techniques. *Nonlinear Dyn.*, 99(1):813–836, 2020.
- [20] Jan R Magnus and Heinz Neudecker. *Matrix differential calculus with applications in statistics and econometrics*. John Wiley & Sons, 2019.
- [21] Eve Marder, Sonal Kedia, and Ekaterina O Morozova. New insights from small rhythmic circuits. *Current opinion in neurobiology*, 76:102610, 2022.
- [22] Erik TK Mau, Michael Rosenblum, and Arkady Pikovsky. High-order phase reduction for coupled 2d oscillators. *Chaos: An Interdisciplinary Journal of Nonlinear Science*, 33(10), 2023.
- [23] J. McKinley, M. Zhang, A. Wead, C. Williams, E. Tognoli, and C. Beetle. Third party stabilization of unstable coordination in systems of coupled oscillators. In *J. Phys. Conf. Ser.*, volume 2090, page 012167. IOP Publishing, 2021.
- [24] R. Milne and F. Guichard. Coupled phase-amplitude dynamics in heterogeneous metacommunities. *J. Theor. Biol.*, 523:110676, 2021.
- [25] Renato E. Mirollo and Steven H. Strogatz. Synchronization of pulse-coupled biological oscillators. *SIAM J. Appl. Math.*, 50(6):1645–1662, 1990.
- [26] Rachel Nicks, Robert Allen, and Stephen Coombes. Insights into oscillator network dynamics using a phase-isostable framework. *Chaos*, 34(1), 2024.
- [27] Edward Ott and Thomas M Antonsen. Low dimensional behavior of large systems of globally coupled oscillators. *Chaos*, 18(3):037113, 2008.
- [28] Y. Park and D. Wilson. High-order accuracy computation of coupling functions for strongly coupled oscillators. *SIAM J. Appl. Dyn. Syst.*, 20(3):1464–1484, 2021.
- [29] Youngmin Park. youngmp/nm: v0.0.1-alpha, September 2024.
- [30] Youngmin Park, Stewart Heitmann, and G. Bard Ermentrout. The utility of phase models in studying neural synchronization. In Ahmed A. Moustafa, editor, *Computational Models of Brain and Behavior*, chapter 36, pages 493–504. Wiley Online Library, 2017.
- [31] Youngmin Park and Dan Wilson. N-body oscillator interactions of higher-order coupling functions. *SIAM Journal on Applied Dynamical Systems*, 23(2):1471–1503, 2024.
- [32] Alberto Pérez-Cervera, Tere M Seara, and Gemma Huguet. Global phase-amplitude description of oscillatory dynamics via the parameterization method. *arXiv preprint arXiv:2004.03647*, 2020.

- [33] Jonathan E Rubin and David Terman. High frequency stimulation of the subthalamic nucleus eliminates pathological thalamic rhythmicity in a computational model. *Comput. Neurosci.*, 16(3):211–235, 2004.
- [34] Richard B Stein, E Roderich Gossen, and Kelvin E Jones. Neuronal variability: noise or part of the signal? *Nature Reviews Neuroscience*, 6(5):389–397, 2005.
- [35] Steven H Strogatz, Daniel M Abrams, Allan McRobie, Bruno Eckhardt, and Edward Ott. Crowd synchrony on the millennium bridge. *Nature*, 438(7064):43–44, 2005.
- [36] Nathaniel Urban and Shreejoy Tripathy. Circuits drive cell diversity. *Nature*, 488(7411):289–290, 2012.
- [37] Dan Wilson. Phase-amplitude reduction far beyond the weakly perturbed paradigm. *Phys. Rev. E.*, 101(2):022220, 2020.
- [38] Dan Wilson and G Bard Ermentrout. Phase models beyond weak coupling. *Phys. Rev. Lett.*, 123(16):164101, 2019.
- [39] Arthur T Winfree. *The geometry of biological time*, volume 12. Springer Science & Business Media, 2001.
- [40] Yunliang Zang and Eve Marder. Neuronal morphology enhances robustness to perturbations of channel densities. *Proceedings of the National Academy of Sciences*, 120(8):e2219049120, 2023.